The Photometric Metallicity and Carbon Distributions of the Milky Way's Halo and Solar Neighborhood from S-PLUS Observations of SDSS Stripe 82

Devin D. Whitten,[1] Vinicius M. Placco,[2,1] Timothy C. Beers,[1] Deokkeun An,[3] Young Sun Lee,[4]
Felipe Almeida-Fernandes,[5] Fábio R. Herpich,[5] Simone Daflon,[6] Carlos E. Barbosa,[5] Hélio D. Perottoni,[5]
Silvia Rossi,[5] Patricia B. Tissera,[7,8] Jinmi Yoon,[9,1] Kris Youakim,[10,11] William Schoenell,[12] Tiago Ribeiro,[13]
and Antonio Kanaan[14]

[1]*Department of Physics and JINA Center for the Evolution of the Elements, University of Notre Dame, Notre Dame, IN 46556, USA*
[2]*Community Science and Data Center/NSF's NOIRLab, 950 N. Cherry Ave., Tucson, AZ 85719, USA*
[3]*Department of Science Education, Ewha Womans University, 52 Ewhayeodae-gil, Seodaemun-gu, Seoul 03760, South Korea*
[4]*Department of Astronomy and Space Science, Chungnam National University, Daejeon 34134, South Korea*
[5]*Departamento de Astronomia, Instituto de Astronomia, Geofísica e Ciências Atmosféricas da USP, Cidade
Universitária, 05508-900, São Paulo, SP, Brazil*
[6]*Observatório Nacional - MCTIC (ON), Rua Gal. José Cristino 77, São Cristóvão, 20921-400, Rio de Janeiro, Brazil*
[7]*Instituto de Astrofísica, Pontificia Universidad Católica de Chile, Av. Vicuña Mackenna 4860, Santiago, Chile*
[8]*Centro de Astro-ingeniería, Pontificia Universidad Católica de Chile, Av. Vicuña Mackenna 4860, Santiago, Chile*
[9]*Space Telescope Science Institute, 3700 San Martin Dr., Baltimore, MD 21218, USA*
[10]*Leibniz-Institut für Astrophysik Potsdam, An der Sternwarte 16, Potsdam 14482, Germany*
[11]*Department of Astronomy, Stockholm University, AlbaNova University Center, SE-106 91 Stockholm - Sweden*
[12]*GMTO Corporation 465 N. Halstead Street, Suite 250 Pasadena, CA 91107, USA*
[13]*Rubin Observatory Project Office, 950 N. Cherry Ave., Tucson, AZ 85719, USA*
[14]*Departamento de Física, Universidade Federal de Santa Catarina, Florianópolis, SC 88040-900, Brazil*

ABSTRACT

We report photometric estimates of effective temperature, $T_{\rm eff}$, metallicity, [Fe/H], carbonicity, [C/Fe], and absolute carbon abundances, A(C), for over 700,000 stars from the Southern Photometric Local Universe Survey (S-PLUS) Data Release 2, covering a substantial fraction of the equatorial Sloan Digital Sky Survey Stripe 82. We present an analysis for two stellar populations: 1) halo main-sequence turnoff stars and 2) K-dwarf stars of mass $0.58 < M/M_\odot < 0.75$ in the Solar Neighborhood. Application of the Stellar Photometric Index Network Explorer (SPHINX) to the mixed-bandwidth (narrow- plus wide-band) filter photometry from S-PLUS produces robust estimates of the metallicities and carbon abundances in stellar atmospheres over a wide range of temperature, $4250 < T_{\rm eff}({\rm K}) < 7000$. The use of multiple narrow-band S-PLUS filters enables SPHINX to achieve substantially lower levels of "catastrophic failures" (large offsets in metallicity estimates relative to spectroscopic determinations) than previous efforts using a single metallicity-sensitive narrow-band filter. We constrain the exponential slope of the Milky Way's K-dwarf halo metallicity distribution function (MDF), $\lambda_{10,{\rm [Fe/H]}} = 0.85 \pm 0.21$, over the metallicity range $-2.5 < {\rm [Fe/H]} < -1.0$; the MDF of our local-volume K-dwarf sample is well-represented by a gamma distribution with parameters $\alpha = 2.8$ and $\beta = 4.2$. S-PLUS photometry obtains absolute carbon abundances with a precision of $\sim 0.35\,{\rm dex}$ for stars with $T_{\rm eff} < 6500\,{\rm K}$. We identify 364 candidate carbon-enhanced metal-poor stars, obtain assignments of these stars into the Yoon-Beers morphological groups in the A(C)-[Fe/H] space, and derive the CEMP frequencies.

Keywords: Galaxy: abundances – Galaxy: stellar content – Galaxy: halo – Galaxy: Solar Neighborhood – techniques: photometric – surveys

1. INTRODUCTION

The metallicity distribution function (MDF) of the Milky Way (MW) halo and Solar Neighborhood is among the most critical observational constraints for models of Galactic chemical evolution (Salvadori et al. 2008). The halo MDF is a manifestation of no less than three fundamental properties of the first stellar generations: the stellar initial mass function, the star-
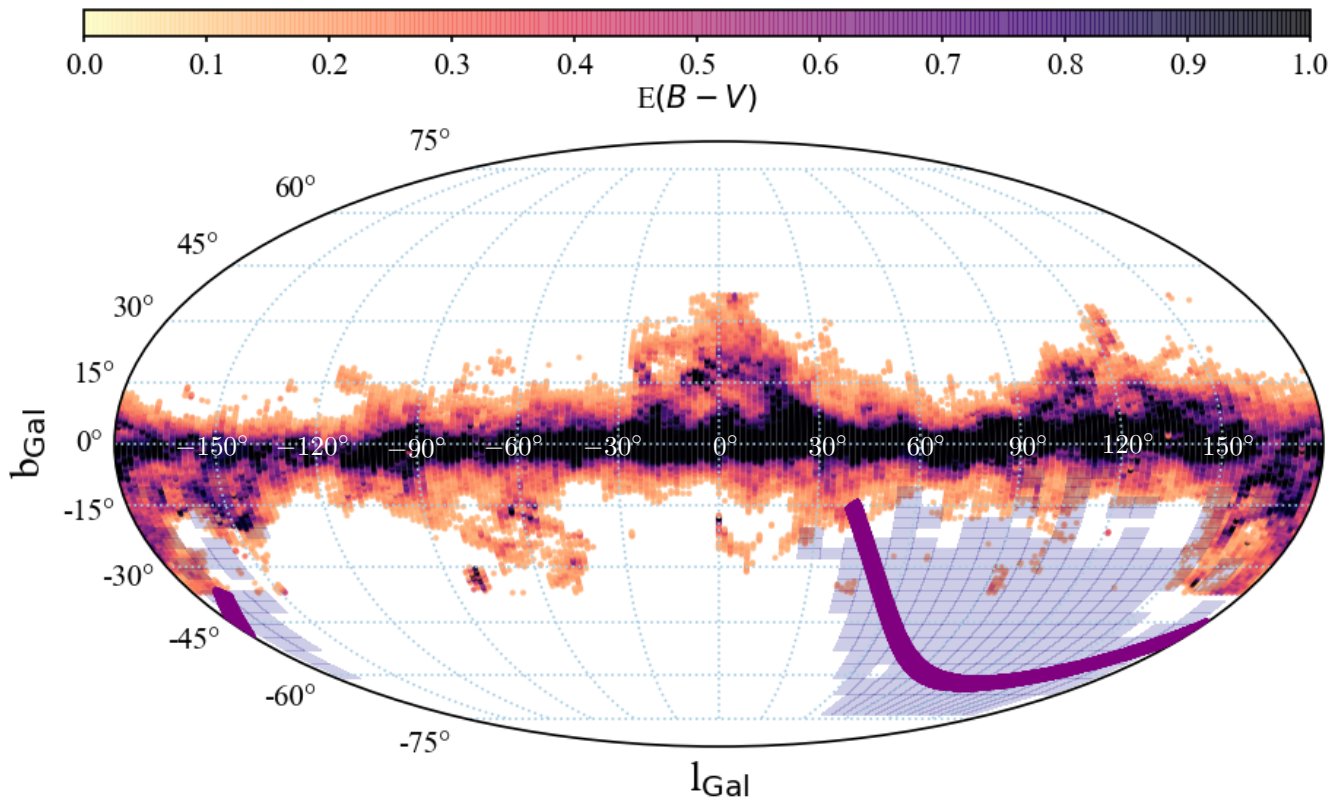
Figure 1. Distribution of the S-PLUS SDSS Stripe 82 sample (*purple*) in Galactic coordinates. The Galactic plane is shown, color-coded by $E(B - V)$, along with the fields sampled by the SEGUE catalog (*blue*) of medium-resolution spectroscopic observations in the Southern Hemisphere (see text for details).

formation history, and the chemical-evolution mechanisms at play in the primordial MW, as well as the contribution of stars to the halo from accreted satellite galaxies. It thus is of considerable importance for understanding the early epochs of Galactic evolution. Historically, Searle & Zinn (1978) were the first to speculate that the formation of the Galactic Halo was much more complex than the rapid, monolithic collapse scenario proposed by the seminal work of Eggen et al. (1962). Searle & Zinn proposed that the halo was formed by transient protogalactic fragments that fell continuously into dynamical equilibrium with the Milky Way after the collapse of its main structural components had been completed (see Dietz et al. 2020, for a more complete discussion of the subject).

In the ΛCDM paradigm, galactic halos are aggregate structures assembled from the successive merging of a large number of sub-galactic fragments. The MDF of the Galactic halo could thus be considered as the sum of each constituent fragment's MDF (Prantzos 2007). These fragments are demonstrably distinct from dwarf spheroidal galaxies (dSphs) *as they appear today*, which fail to reproduce the fractions of low-metallicity stars seen in the halo (Helmi et al. 2006; Prantzos 2007).

The observed discrepancies between the Milky Way's halo MDF and elemental-abundance ratios with those of canonical dSph galaxies such as Fornax, Sculptor, Sextans, and Carina present a challenge to models of Galactic evolution that presume a hierarchical assembly of early merging dwarf galaxies (Tolstoy et al. 2009). Attempts to rectify these differences suppose a pre-enrichment mechanism in the dSph birth environment (Helmi et al. 2006; Salvadori et al. 2008), although this process is not yet clearly understood, and must necessarily have been quite rapid to have taken place before the onset of star formation.

In contrast, ultra-faint dwarf galaxies (UFDs) have been demonstrated to possess populations of [Fe/H] < -3.0[1] stars (Kirby et al. 2008; Brown et al. 2014), suggesting that (surviving) UFDs may be more similar to the accreted building blocks that formed the metal-poor tail of the Galactic stellar halo (Frebel et al. 2010; Simon 2019). However, both the relatively small number

---

[1] Relative abundance ratios used in this work correspond to [A/B] = $\log(N_A/N_B) - \log(N_A/N_B)_\odot$, where N indicates the number density of the given species.

of known UFDs, as well as their sparse and faint member stars, present challenges to carry out comprehensive population studies. Observations of the numerous, relatively bright, field stars of the MW's constituent halo populations may thus provide a superior means for probing the Galaxy's progenitor systems.

Chemical-evolution modeling has, in the past, considered the MDF of G-dwarf stars as a primary observational constraint (e.g., Caimmi 2008, and references therein). These low-mass ($0.8 < M/M_\odot < 1.1$) stars possess main-sequence lifetimes older than the disk age, regardless of their metallicity (Bovy et al. 2012), although some G dwarfs may be massive enough to have already evolved away from the main sequence (Kotoneva et al. 2002). However, Fenner & Gibson (2003) suggests that K-dwarf stars ($0.5 < M/M_\odot < 0.8$) are perhaps more directly comparable, as their lower masses render the population less susceptible to stellar evolutionary effects. Models constrained by the G-dwarf MDF suggest a "two-infall" scenario, with a long timescale for thin-disk formation (Chiappini et al. 2001). These comparatively long-lived stars present an opportunity to study the chemical distributions of the Solar Neighborhood, while mitigating evolutionary effects and age biases in their selection.

Previous work (e.g., Schörck et al. 2009; Li et al. 2010) relied on comparisons to the halo MDFs obtained by spectroscopic surveys such as the Hamburg-ESO survey (HES; Christlieb 2003). More recently, studies (e.g., Carollo et al. 2007; Carollo et al. 2010; Beers et al. 2012; Lee et al. 2017; Yoon et al. 2018; Carollo et al. 2019; Kim et al. 2019; Lee et al. 2019) have transitioned to spectroscopic surveys of much larger numbers of halo stars, most notably the Sloan Digital Sky Survey (SDSS; York et al. 2000) and its extensions, the Sloan Extension for Galactic Understanding and Exploration (SEGUE; Yanny et al. 2009), the Baryon Oscillation Spectroscopic Survey (BOSS; Dawson et al. 2013), and the Apache POint Galactic Evolution Experiment (APOGEE; Majewski et al. 2017). Nevertheless, such spectroscopic surveys suffer from incompleteness and bias to various degrees, and can be subject to difficult-to-model selection functions.

While some studies, such as Bovy et al. (2012) and others (Mints & Hekker 2019, and references therein), have sought to unravel the effects of spectroscopic-survey selection effects, photometric surveys can substantially reduce these effects, while also sampling a significantly larger fraction of the sky. Using a technique based on broad-band SDSS *ugriz* photometry, An et al. (2013) found that, when the resulting halo photometric MDF is de-convolved into two Gaussian components

(with peaks at [Fe/H] = -1.7 and -2.3), the more metal-poor component accounts for $20-35\%$ of the halo population within the distance range $d \sim 5-8$ kpc from the Sun. It should be noted that this study was limited to main-sequence dwarfs over a restricted range of stellar mass in order to minimize metallicity-related luminosity effects, whereby metal abundance can significantly affect the luminosity of stars and impose a bias on magnitude-limited samples. Based on the "depth optimized" co-added sample of SDSS Stripe 82 data from Jiang et al. (2014), An et al. (2015) extended the photometric metallicity estimates of stars out to $d \sim 10.5$ kpc, largely due to inclusion of a fainter u-band limit. When their new photometric MDF was de-convolved into multiple populations, with peak metallicities of [Fe/H] = -1.4 and [Fe/H] = -1.9, the more metal-poor component was found to constitute $\sim 35-55\%$ of halo stars in the Solar Neighborhood.

The advent of recent photometric surveys employing mixed-bandwidth photometric filters targeting key absorption features, such as the Ca II lines[2], have significantly expanding the metallicity sensitivity of photometric surveys. Examples include SkyMapper (Keller et al. 2007) and *Pristine* (Starkenburg et al. 2017). Youakim et al. (2020) recently investigated the MDF of main-sequence turnoff (MSTO) stars, extending the metal-poor tail to [Fe/H] ~ -3.4, and constraining the slope of the low-metallicity tail of the halo MDF to $\Delta(\log N)/\Delta([\mathrm{Fe/H}]) = 1.0 \pm 0.1$. Interestingly, this result is consistent with the very early work from Beers (1987), based on only ~ 130 metal-poor stars from the HK survey (Beers et al. 1985).

The Javalambre and Southern Photometric Local Universe Surveys (J-PLUS; Cenarro et al. 2019, S-PLUS; Mendes de Oliveira et al. 2019), are poised to further expand the metallicity sensitivity of photometric studies, as well as to open up the possibility of measuring other elements of importance, such as C and Mg, with the implementation of the Javalambre filter system of 7 narrow-band and 5 wide-band filters (Marín-Franch et al. 2012), and a planned combined footprint of over $17,000 \deg^2$[3] In Whitten et al. (2019a), the Stellar Pho-

---

[2] This technique was first explored in a series of papers beginning with Anthony-Twarog et al. (1991), with improved calibrations at lower metallicity by Anthony-Twarog et al. (2000).

[3] A total of $8,500 \deg^2$ and $9300 \deg^2$ for J-PLUS and S-PLUS, respectively. J-PLUS and S-PLUS are performed by two 80-cm telescopes called T80/JAST and T80-South, respectively. T80-South and its large-format camera, including the filters (see www.splus.iag.usp.br), located at Cerro Tololo Interamerican Observatory, are a duplicate of the T80/JAST system, installed at Cerro Javalambre (see www.jplus.org for details).
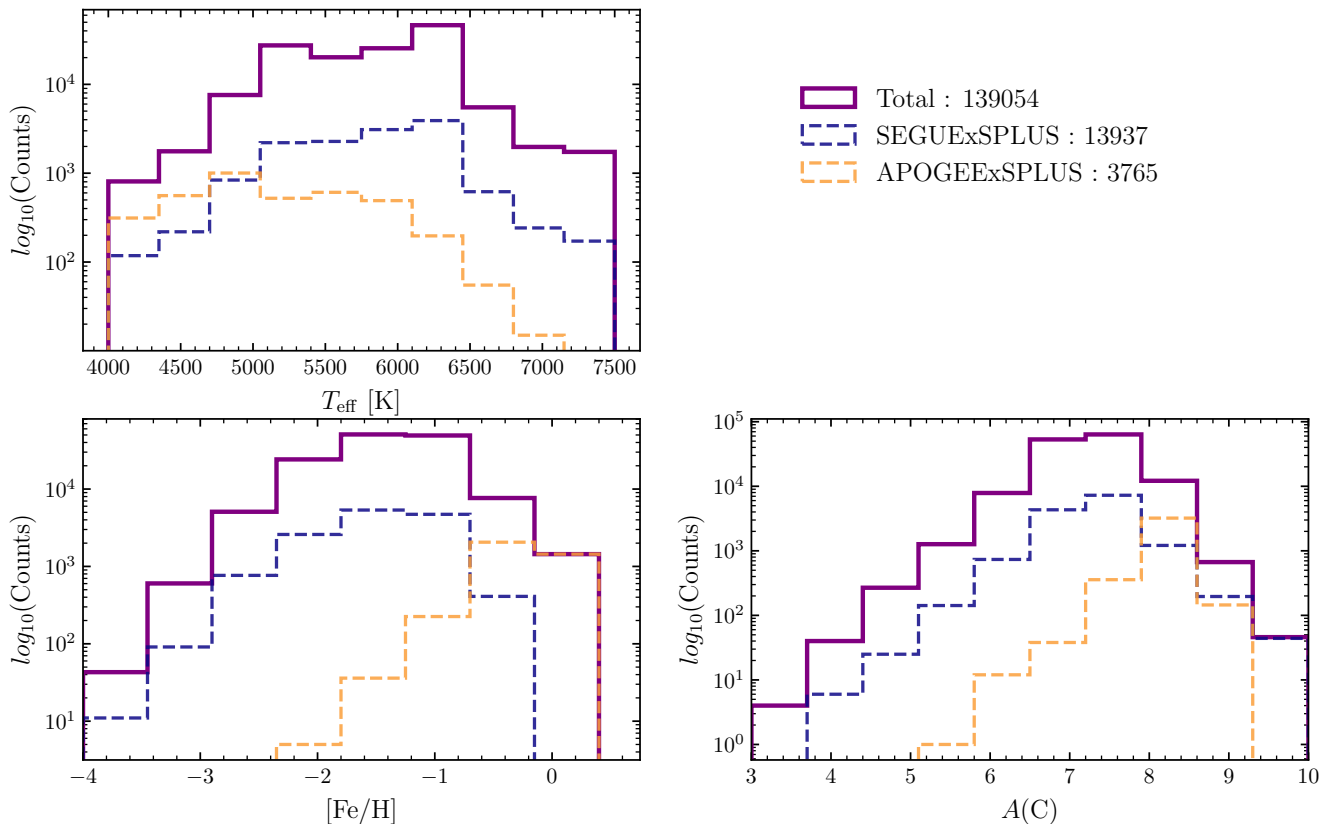
Figure 2. Distributions of T_{eff} (top left panel), [Fe/H] (bottom left panel), and A(C) (bottom right panel) of the spectroscopic training catalog. The total distribution (*purple*) is shown for each parameter, along with the contributions from the constituent spectroscopic catalogs, SEGUE (*blue*) (which includes legacy SDSS, SEGUE, SEGUE-2, and BOSS) and APOGEE (*orange*), crossed-matched with the S-PLUS (*dashed*) photometric catalog.

tometric Index Network Explorer (SPHINX) was demonstrated to be an effective means of utilizing the 12-band filter system used in J-PLUS and S-PLUS to produce reliable estimates of effective temperature and metallicity for stars, based on the relatively small amount of data then available.

In this paper, we employ SPHINX to study the metallicity ([Fe/H]), carbonicity ([C/Fe]), and absolute carbon abundance (A(C)) distributions for two S-PLUS photometric samples of stars from SDSS Stripe 82 – MSTO stars and cooler main-sequence K-type dwarfs. In Section 2, we describe the photometric and spectroscopic catalogs used in this work. In Section 3, we detail the structure and training procedure of SPHINX to produce photometric estimates of effective temperature, T_{eff}, metallicity, [Fe/H], and absolute carbon abundance, A(C)[4]. We describe the selections made from the S-PLUS Stripe 82 data release to produce a MSTO and a

mass-selected local K-dwarf sample in Section 4. Finally, we discuss the results of the metallicity and carbonicity distributions and their analyses for both samples in Section 5, compare with a number of previous efforts, and call particular attention to the issue of "catastrophic failures" in photometric estimates of metallicity (which our SPHINX analysis of S-PLUS data greatly decreases). Concluding remarks are provided in Section 6.

2. CATALOGS

In this section, we describe the S-PLUS Stripe 82 data release employed in this work, and the spectroscopic catalogs used to train and test our derived estimates of stellar T_{eff}, [Fe/H], and A(C). Note that the carbon-to-iron ratio, or carbonicity, [C/Fe], is directly obtained from A(C) and [Fe/H]: [C/Fe] = A(C) − [Fe/H] − A(C)$_\odot$ (where A(C)$_\odot$ = 8.43; Asplund et al. 2009).

2.1. *S-PLUS Stripe 82*

S-PLUS is an ongoing survey, mapping 9,300 deg^2 of the Southern sky with the Javalambre filter system comprising an optical 12-band narrow- and broad-band pho-

---

[4] A(C) = $\log \epsilon$ (C) = $\log(N_C/N_H) + 12$, where N represents the number densities of each species.

tometric system, including five broad-band *ugriz* filters analogous to the SDSS. S-PLUS employs a dedicated 0.8 m telescope (T80S) located on Cerro Tololo, Chile. The imager, T80Cam, hosts a 9232×9216 $10\,\mu$m-pixel array, with a $1.4° \times 1.4°$ field-of-view. The public data release[5] of S-PLUS Stripe 82 (Mendes de Oliveira et al. 2019) comprises 170 co-added fields covering a total of $336\,\mathrm{deg}^2$ from $4^h <$ R.A. $< 20^h$ and $-1.26° <$ Decl. $< +1.26°$, collected between 2016 and 2018. The S-PLUS raw data are reduced using an adapted early version (number 0.9.9) of the data-processing pipeline JYPE (see Cristóbal-Hornillos et al. 2014, for details), developed by CEFCA's Unit for Processing and Data Archiving, UPAD. This code was designed to reduce data for two surveys, J-PLUS (Cenarro et al. 2019) and J-PAS (Bonoli et al. 2020, submitted), and is based on the photometric pipeline originally developed for the ALHAMBRA survey (see Cristobal-Hornillos et al. 2009; Molino et al. 2014).

The final magnitude-limited catalog includes $700,000+$ sources down to $r = 21$ on the AB system. This preliminary catalog is then cleaned of galaxies and other problematic sources (i.e., close double stars, image defects, etc.) via a stellar-probability procedure based on a random forest algorithm (Costa-Duarte et al. 2019). Only objects with a 90 % confidence of being stellar sources (as per DR1) were accepted. The extent of the S-PLUS Stripe 82 sample is shown in Figure 1, along with the Galactic plane and the spectroscopic training and validations samples discussed below.

The Javalambre filter system possesses narrow- and intermediate-band filters of particular interest to stellar-parameter determinations. We refer the interested reader to Marín-Franch et al. (2012), Cenarro et al. (2019), and Mendes de Oliveira et al. (2019) for an in-depth discussion of this 12-filter system, but highlight three such filters here. The *J*0410 filter ($\Delta\lambda = 201$ Å) is centered on the Hδ Balmer line ($\lambda = 4102$Å), which exhibits effective-temperature dependence. The *J*0395 filter ($\Delta\lambda = 103$ Å) is centered directly on the Ca II H & K lines, which have been used extensively for determinations of metallicity in low- and medium-resolution spectroscopy. Finally, the *J*0430 filter ($\Delta\lambda = 200$ Å) is positioned on the CH *G*-band, a useful molecular feature for carbon-abundance determination, also used by previous medium- and high-resolution spectroscopic surveys. We note that the Javalambre *J*0395 filter is similar to the Pristine Ca II H & K filter (Starkenburg et al. 2017), which has been successfully used to

search for low-metallicity stars. These better isolate the metallicity-sensitive features than the intermediate-band filters from, e.g., SkyMapper (*v* filter, Bessell et al. 2011; Wolf et al. 2018)

2.2. *Spectroscopic Catalogs*

Here we describe the spectroscopic sources used to obtain stellar parameters for training and validation purposes. Figure 2 shows the distribution of stellar atmospheric parameters T_{eff} and [Fe/H], as well as the absolute carbon abundance, $A(\mathrm{C})$, available for network training for each of the catalogs described below.

2.2.1. *SEGUE*

The primary catalog employed for network training of the S-PLUS photometric data is derived from the SEGUE (Yanny et al. 2009) and SEGUE-2 (Rockosi et al., in prep.) surveys. We also include observations taken as part of the SDSS Legacy Survey (Abazajian et al. 2009), as well as from BOSS (Dawson et al. 2013). For simplicity of notation, we refer to the complete set of these data as the SEGUE sample, since it is the dominant contributor. By application of the SEGUE Stellar Parameter Pipeline (SSPP, Lee et al. 2008a,b), atmospheric parameters and estimates of [Fe/H] and $A(\mathrm{C})$ are obtained for the $\sim 300,000$ stars in common with available spectroscopy. The S-PLUS Stripe 82 sample was then cross-matched with this catalog using a search radius of $5''$, resulting in 23,882 stars with available S-PLUS photometry and SEGUE/SSPP stellar atmospheric parameters. We utilize this spectroscopic sample for comparison to our photometric measurements with S-PLUS.

2.2.2. *APOGEE*

To extend the metallicity range of our photometric training sets, in particular for more metal-rich stars, we include a subset of stars from APOGEE (Majewski et al. 2017). APOGEE is a high-resolution ($R \sim 22,500$), near-infrared ($1.5-1.7\,\mu$m) stellar spectroscopic survey performed at both the Apache Point Observatory in New Mexico, USA, using the APOGEE-North spectrograph on the 2.5-meter Sloan Foundation Telescope, and, as of Dec 2019, at Las Campanas Observatory, using the essentially identical APOGEE-South spectrograph. Chemical abundances produced with the APOGEE Stellar Parameters and Abundances Pipeline (ASPCAP; García Pérez et al. 2016) serve as the primary catalog for our sources with [Fe/H] > -0.5. While the SEGUE and APOGEE cross-matches have a similar number of stars with [Fe/H] > -0.5 ($\sim 5,000$), the higher resolution and typically much higher signal-to-noise ratios of the APOGEE spectra are expected to yield su-

---

[5] Available at https://datalab.noao.edu/splus/

perior results to those of SEGUE for [Fe/H] > −0.5 (Mészáros et al. 2013). We note a small systematic off-set, $[Fe/H]_{SEGUE} − [Fe/H]_{APOGEE} = −0.09$ dex, between the metallicity reported by ASPCAP and the biweight metallicity estimate adopted from the SSPP. We adjust the ASPCAP metallicities to remove this offset in the master catalogs employed in the [Fe/H] and $A(C)$ training exercise. A larger offset is seen in the $A(C)$ values, $A(C)_{SEGUE} − A(C)_{APOGEE} = −0.21$ dex. This offset is also corrected for, and we note that stars from APOGEE represent only ∼15% of total stars in the training samples.

2.2.3. *Sample Contamination*

We address possible contamination of our photometric samples from S-PLUS by background quasars via cross-matching with the Large Quasar Astrometric Catalog (Gattano et al. 2018). This catalog consists of nearly all known quasars, with the addition of recent identifications in the SDSS DR12Q, as well as *Gaia* DR1 (Gaia Collaboration et al. 2016). We find 9,238 matches in the S-PLUS Stripe 82 sample, which were removed from all subsequent analysis.

We additionally note the potential for contamination by cool white dwarfs in our samples. While the vast majority of white dwarfs that could be present in our data are substantially hotter than the temperature selection implemented for both the MSTO and K-dwarf samples, cooler ($T_{eff} < 10000$) white dwarfs can occupy a similar $(g − i)_0$ range as the MSTO sample. White dwarfs possess significantly higher surface gravity than MSTO or K-dwarf stars, $\log g > 7$ (Eisenstein et al. 2006). They can thus be effectively excluded by the color restriction $(u − g)_0 > 0.6$, as $(u − g)_0$ is a known surface-gravity dependent feature, due to the Stark pressure broadening (and overlap) of Balmer lines in the near-UV region. Finally, white dwarfs are intrinsically faint, which severely limits the distance range within which white dwarfs can populate our samples. We conclude that white dwarfs are not a significant source of contamination on our sample selections.

The main samples selected in this work consist of warm MSTO stars and cool K-dwarf stars. We estimate the extent to which these samples are contaminated by giants from an absolute magnitude (M_g) calibration using the subset of the S-PLUS Stripe 82 sample cross-matched with *Gaia* DR2 (Gaia Collaboration et al. 2018a), using a search radius of 5″. Of the 36,630 stars with acceptable quality S-PLUS photometry and *Gaia* astrometry, ∼ 14% possess a $M_g > 4$. Giant contamination is primarily a concern for the K-dwarf sample, where the contamination is determined to be ∼ 25%.

We address the measures taken to mitigate this factor in the sample selection in §4 below.

SDSS Stripe 82, was, by design, frequently revisited during the course of the various SDSS spectroscopic surveys. Thus, our spectroscopic catalogs were internally cross-matched with a search radius of 2″ to identify duplicate observations. In the event of a duplicate observation, the spectrum with the highest S/N ratio is chosen. Approximately 23% of SEGUE sources were found to have duplicate spectroscopic observations. These stars were included for training purposes, as they are legitimate sources. For the determinations of chemical-abundance distributions described in §5 below, these stars were removed.

2.3. *Photometric Calibration of S-PLUS Observations*

The sample used in this paper is a revision of the S-PLUS DR1, where a new calibration of the data was employed. The technique used for calibration is the same as that of DR1, described in Mendes de Oliveira et al. (2019). It relies on fitting stellar templates to a reference catalog (in this case, SDSS; Ivezić et al. 2007) in order to predict the S-PLUS calibrated magnitudes for a selection of stars. Then, the zero-points are derived from the differences between the instrumental and the predicted magnitudes. The main differences between the S-PLUS DR1 and the revised DR1 sample used here are that (i) in the latter an aperture correction was applied to the 3″ magnitudes before calibration, and (ii) the revised calibration used a library of theoretical stellar spectra (Coelho 2014), instead of the empirical library used for DR1. These changes, as well as a more detailed description of the calibration process, are discussed in the upcoming S-PLUS DR2 paper (Almeida-Fernandes et al., in prep.). Extinction corrections were performed on this catalog, using $E(B − V)$ values from Schlafly & Finkbeiner (2011), based on the Schlegel et al. (1998) dust map, and extinction coefficients from López-Sanjuan et al. (2019). This dust map is shown in comparison with the S-PLUS Stripe 82 footprint in Figure 1.
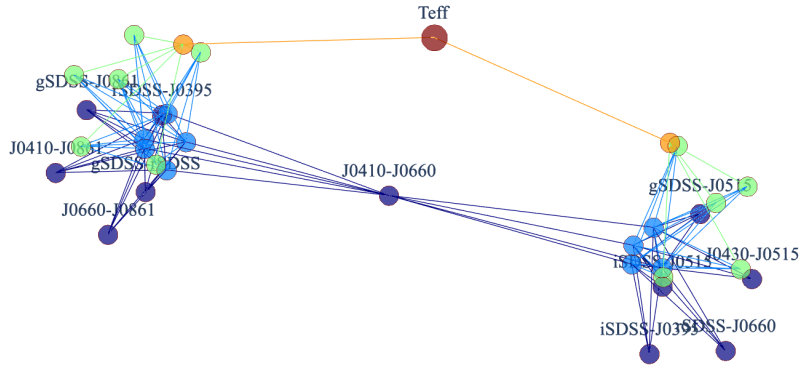
3. PROCESSING WITH SPHINX

Here we describe the basic operations and training procedures of SPHINX. We refer the interested reader to the more complete descriptions in Whitten et al. (2019a).
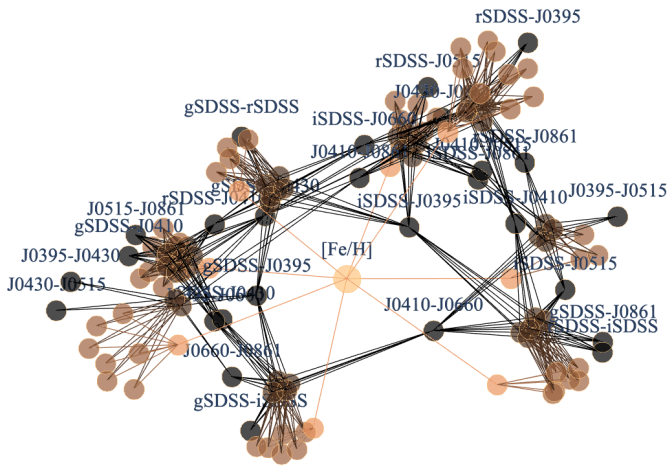
3.1. *Generative Network Training*

SPHINX is essentially an Artificial Neural Network (ANN) consensus procedure, consisting of a network of
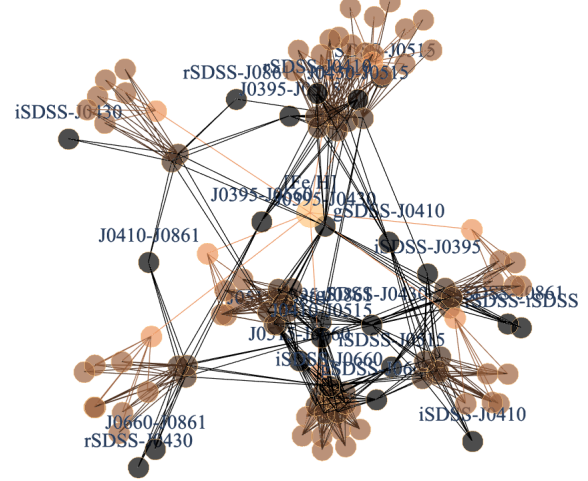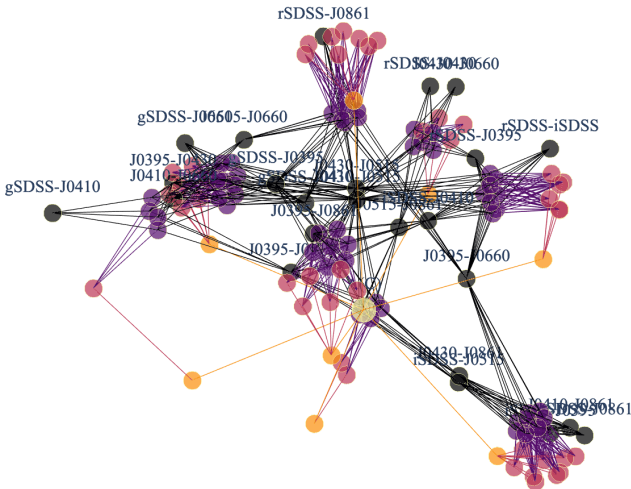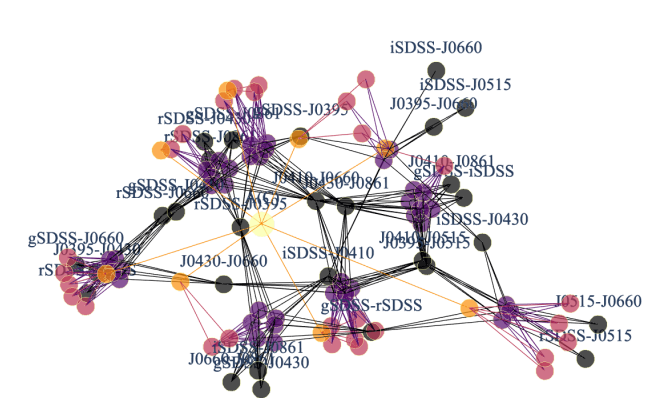
Figure 3. Architecture of the generative training process for the effective temperature ($T_{\rm eff}$) network (upper panel), the metallicity ([Fe/H]) networks (split into two $T_{\rm eff}$ regimes, as indicated in the legend), and the absolute carbon (A(C)) network, split into the same $T_{\rm eff}$ regimes. Black dots indicate the photometric color inputs, and remaining colors indicate successive layers in each model. See text for more details. For a description of the filters, see http://www.splus.iag.usp.br/instrumentation/

ANN sub-units, each with a unique combination of S-PLUS mixed-bandwidth photometric colors. Each ANN sub-unit is generated in a stochastic manner, whereby the number of nodes, the activation function, and the solution algorithm are randomly assigned, subject to a number of conditions. First, the [Fe/H] and $A(C)$ ANN sub-units are restricted to two hidden layers; the addition of more hidden layers produced no notable improvements in the model's predictive power. Each ANN sub-unit is designated one of the following activation functions at random: identity, hyperbolic tangent, logistic, and the rectified linear unit. We additionally randomize the solution function implemented in each sub-unit: the optimized gradient-based algorithm *Adam* (Kingma & Ba 2014), Limited-memory Broyden-Fletcher-Goldfarb-Shanno algorithm (L-BFGS), and the conventional Stochastic Gradient Descent (SGD). The number of color inputs to each ANN sub-unit is fixed at six, with each ANN sub-unit receiving a unique combination of the available colors. Finally, for each respective stellar-parameter network ($T_{\rm eff}$, [Fe/H], and $A(C)$), we force the inclusion of that parameter's most sensitive narrow-band filter in all of its constituent ANN sub-units, corresponding to $J0410$, $J0395$, and $J0430$, for the $T_{\rm eff}$, [Fe/H], and $A(C)$ networks, respectively.

All of the ANN sub-units are then trained on $\sim 2,000$ sub-samples from the SEGUE calibration set, including APOGEE, selected by uniformly sampling the parameter in question. The effective temperature network is trained across the range $4000 < T_{\rm eff}({\rm K}) < 7500$, the metallicity network is trained across $-3.5 < [{\rm Fe/H}] < +0.2$, and the absolute carbon abundance network is trained across $5.00 < A(C) < 8.75$. We found during training that $A(C)$ estimates were infeasible for stars with $T_{\rm eff} > 6500\,{\rm K}$, due to the minimal impact of carbon on the filter set for such warm stars. This limitation prevents consideration of the carbon abundances for our full MSTO sample, but no such difficulty exists over the effective temperature range of our K-dwarf sample.

Validation scores are determined for each network according to the average residual, evaluated with an independent validation set. For each parameter network, the top eight ANN sub-units are selected from the ensemble. These optimized ANN sub-units are shown in Figure 3 for [Fe/H] and $A(C)$, where we visualize the aggregate network using the Kamada-Kawai algorithm (Kamada & Kawai 1989). These validated ANN sub-units form the basis of the consensus method for parameter determination used throughout this work, where final parameter estimates are the average of the ANN sub-unit estimates, weighted by the validation scores. For both metallicity and absolute carbon abundance,

separate networks are constructed and trained for cool $4200 < T_{\rm eff}({\rm K}) < 5750$ and warm $5500 < T_{\rm eff}({\rm K}) < 7000$ stars. Stars are directed to each effective temperature partition using the SPHINX $T_{\rm eff}$ estimate. For stars in the intermediate region, $5500 < T_{\rm eff}({\rm K}) < 5750$, estimates from both networks are merged, and the average of the two estimates is taken.

The uncertainties reported for the [Fe/H] and $A(C)$ estimates are based on the scatter amongst the individual ANN sub-units in each network. While representative of the uncertainty of the estimation procedure, these values were found to be quite low, and are unlikely to reflect the underlying scatter seen in the spectroscopic validation stars, $\sigma([{\rm Fe/H}]) = 0.25\,{\rm dex}$ and $\sigma(A(C)) = 0.35\,{\rm dex}$, respectively. We obtain a final estimate of the uncertainty in these estimates by adding the standard deviation of the spectroscopic residuals and the uncertainties reported from SPHINX in quadrature. We discuss validations of the $A(C)$ determinations from SPHINX in the following subsection.

3.2. *Absolute Carbon Validation*

The effective temperature and metallicity determinations from SPHINX were validated in Whitten et al. (2019a), and we refer the interested reader to the details therein. Here, we investigate the $A(C)$ determinations developed in this work. In Figure 4, the $A(C)$ residuals – defined as the difference between the photometric value determined with SPHINX and the adopted spectroscopic estimate – are shown plotted against four parameters of particular interest. The $A(C)$ residual is shown as a function of the g-band magnitude in the top left panel of Figure 4, along with the spectroscopic $A(C)$ estimate (top right panel), the reddening estimate $E(B-V)$ (bottom left panel), and finally the photometric effective temperature produced with SPHINX (bottom right panel). For the g-band magnitude, reddening, and effective temperature, any trends seen in the $A(C)$ estimates are well within the standard deviation in the $A(C)$ residuals, $\sigma(A(C)) = 0.35\,{\rm dex}$.

We note the apparent trend in the $A(C)$ residuals with the reddening, $E(B-V)$. However, the majority of stars in our samples possess reddening values less than $E(B-V) < 0.1$, with a maximum of $E(B-V) < 0.15$. As this trend is within the standard deviation of the $A(C)$ residuals, we do not impose a correction on the photometric $A(C)$ values determined with SPHINX. This is partly due to the nature of the $E(B-V)$ values utilized in this work, namely the Schlafly & Finkbeiner (2011) recalibration of Schlegel et al. (1998), which do not take distance into account. While 3-D estimates have been produced to take into account the line-of-sight distance,

for instance the work of Green et al. (2019) based on *Gaia*, Pan-STARRS, and 2MASS, these estimates are currently limited to declinations with $\delta > -30°$, and ultimately rely on high-quality distance estimates, which can introduce a significant amount of uncertainty. Finally, a trend in the $A(\mathrm{C})$ residual with the spectroscopically determined $A(\mathrm{C})$ value is seen in Figure 4. Below $A(\mathrm{C}) < 6.0$, photometric estimates are seen to over-estimate the spectroscopic value. Above $A(\mathrm{C}) > 8.0$, the photometric values under-estimate the carbon abundance, compared with the spectroscopically determined values. Further investigation revealed no clear origin for this trend, beyond the difficulties inherent in carbon estimation, namely the nascent saturation of carbon features beyond $A(\mathrm{C}) > 8.5$, as discussed in Yoon et al. (2020). We emphasize the preliminary nature of the photometric carbon abundances produced in this work, where we implement a threshold for absolute carbon estimates of $A(\mathrm{C}) < 8.5$, and reserve further refinements of the photometric $A(\mathrm{C})$ determinations to future studies.

4. SAMPLE SELECTION

Here we describe the stellar isochrones we employ, and the various criteria adopted to select MSTO stars and K-dwarf stars from the S-PLUS Stripe 82 data release.

4.1. *Stellar Isochrones*

The stellar isochrones used in this work were produced from the Yonsei-Yale (YY; Demarque et al. 2004) models, which take into account helium diffusion and convective-core overshoot. Isochrones were generated in the range [Fe/H] = [−4.0, 0.0] and ages of 10, 11, and 12 Gyr, where we linearly interpolated between models as necessary. For all models, the α-element abundance ratio was set to [α/Fe] = +0.4. These models were transformed to equivalent SDSS photometry via the Johnson-Cousins to SDSS calibrations of Jordi et al. (2006).

For validation purposes, we make use of distances computed with StarHorse (Anders et al. 2019), which combines parallax estimates and optical photometry from *Gaia* DR2 with photometric catalogs from Pan-STARRS, 2MASS, and AllWISE, to produce Bayesian distance estimates for 265 million stars brighter than $G = 18$[6]. Distance estimates from StarHorse were limited to those for which the fractional posterior uncertainty was $(d_{84} - d_{16})/d_{50} < 0.3$, where d_{84} and d_{16} are the 84th and 16th percentiles, respectively.

4.2. *Main-Sequence Turn-off Selection*

We select MSTO stars from the S-PLUS Stripe 82 catalog primarily on the basis of effective temperature, with an additional $(g-i)_0$ selection. Figure 5 shows the temperature-selection window, corresponding to 12 Gyr isochrones.

For the calibration of our selection function, absolute magnitudes, M_g, are determined using distance estimates obtained by StarHorse. We select MSTO stars within the range $6000 < T_{\mathrm{eff}}(\mathrm{K}) < 7000$. This sample is additionally subjected to a restriction on the vertical distance from the Galactic plane, $|Z| > 3\,\mathrm{kpc}$. As distance estimates from StarHorse are not available for the majority of the stars in our sample, the spatial coordinates are determined via an approximate distance modulus, whereby an absolute magnitude $M_g = 4$ for the MSTO sample was uniformly adopted. Additionally, a Galactic latitude limit of $|b| > 30°$ was applied to mitigate contamination from the disk system. Of the 88,469 stars with acceptable S-PLUS photometry and SPHINX metallicities, our final MSTO sample consisted of 6,360 stars. An identical selection was performed on our SEGUE spectroscopic catalog to produce a sample of 4,038 stars.

4.3. *Mass-Based K-Dwarf Selection*

In addition to the effective-temperature selection for MSTO stars, we conduct a selection on mass for main-sequence K-dwarf stars in the range $0.58 < M/M_\odot < 0.75$. This is done for several reasons. First, this region of stellar mass corresponds to a color-space selection in $(g-i)_0$ and $(u-g)_0$ that is effectively independent of age. Stars selected on mass in this manner are therefore unbiased towards any particular age. Secondly, we can compare the validity of our chemical-abundance distributions to the work of An et al. (2015), which implemented a similar mass range, $0.65 < M/M_\odot < 0.8$. Lastly, this mass range corresponds to an effective-temperature range $(4250 < T_{\mathrm{eff}}(\mathrm{K}) < 6250)$ that permits confident photometric estimations of stellar carbon abundance, in addition to metallicity.

Our mass-based selection comprises a three-dimensional criteria: T_{eff}, $(g - i)_0$[7], and [Fe/H]. We develop the selection region on the basis of 12 Gyr stellar isochrones, in conjunction with a Support Vector Machine (SVM), in order to robustly determine the 3-D contour region populated by the stars in this mass range.

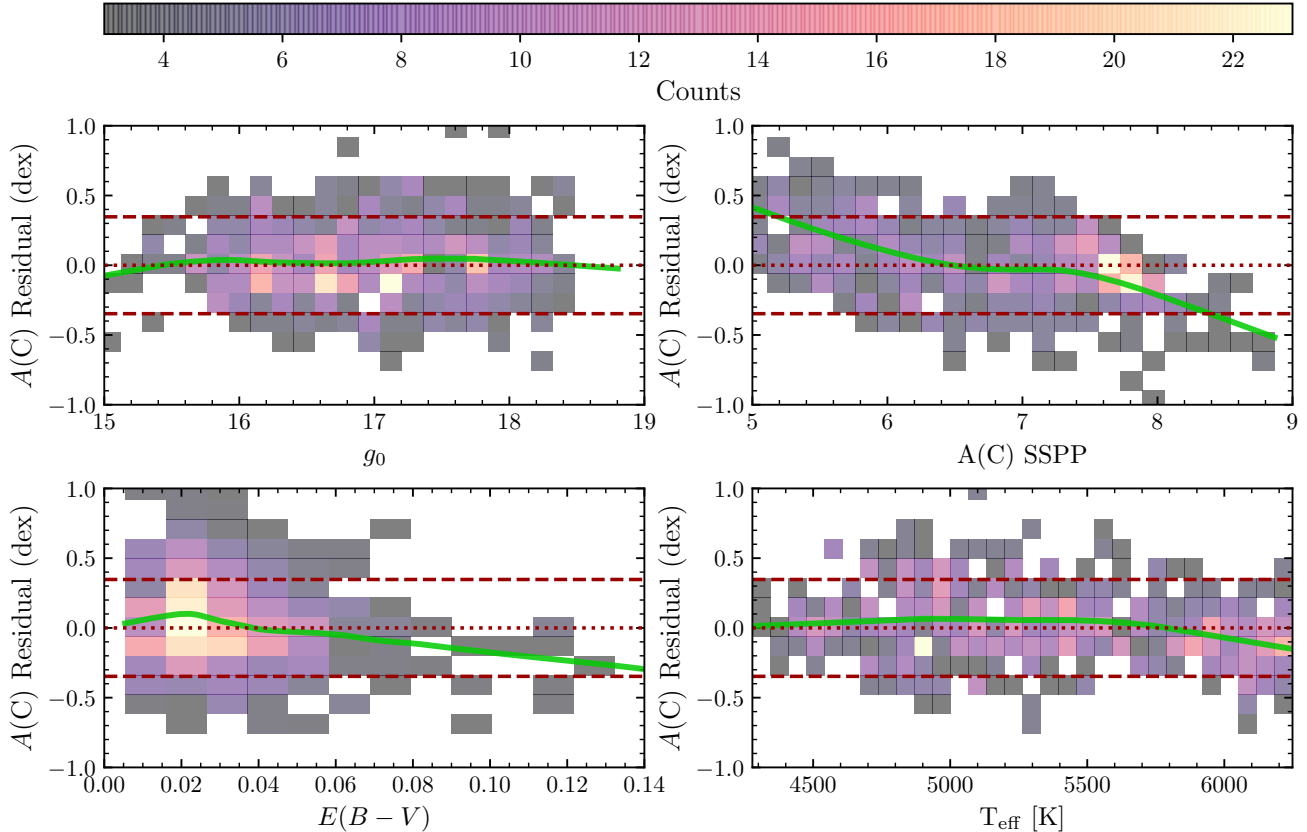[7] The reddening treatment is the same as the one described in Section 3.2.

Figure 4. A(C) residual trends in validation samples with `SPHINX`. The difference between the `SPHINX` photometric A(C) estimate and the spectrscopically determined values are shown plotted against the g magnitude (top left panel), the spectroscopic A(C) value (top right panel), the reddening, $E(B-V)$ (bottom left panel), and the photometric effective-temperature estimate (bottom right panel). Trend-lines (green panel) are determined via locally weighted regression.

To simulate the expected uncertainty inherent in the spectroscopic SEGUE and photometric catalogs, we inject the YY stellar isochrones with random noise according to the following: $\sigma(T_{\mathrm{eff}}) = 100\,\mathrm{K}$, $\sigma(g - i)_0 = 0.2\,\mathrm{mag}$, and $\sigma([\mathrm{Fe/H}]) = 0.3\,\mathrm{dex}$. These noise-injected isochrones form the basis of our decision function.

The isochrones are then reduced to a mass range corresponding to $0.57 < M/M_\odot < 0.75$. To train our SVM on the decision boundary, we first subject the isochrone parameters T_{eff}, $(g - i)_0$, and [Fe/H] to Principal Component Analysis (PCA), in order to maximize the statistical variance along each of the transformed principal axes, while centering the distribution and scaling the inputs to unity variances.

We adopt a similar SVM training methodology to that described in Whitten et al. (2019b), namely a radial basis function. The width of the radial basis function, γ, is set to the variance of the training set. We additionally weight the cost function by the inverse of the class frequencies in our training set, consisting of $\sim 7,900$

positive examples, and $\sim 7,600$ negative samples. Negative examples were assembled by embedding the positive mass-selected isochrone sample in a surrounding mesh. Surrounding the positive examples from the isochrone ensures a closed contour following SVM training.

The resulting decision boundary for the mass selection is shown in Figure 6. In the left panel, the YY isochones that formed the basis of the decision boundary are shown in gray. In the right panel, we overlay the sub-sample of the S-PLUS Stripe 82 catalog with mass estimates from `StarHorse`.

We note that, particularly for higher values of metallicity, $[\mathrm{Fe/H}] > -1.0$, some contamination from giant-branch stars is present within the selection region. Using the subset of the S-PLUS Stripe 82 with spectroscopic surface-gravity estimates from SEGUE, we estimate the contamination level to be $\sim 25\%$. However, Thomas et al. (2019) demonstrated the capability of Random Forest Classifiers (RFCs) to discriminate between dwarfs and giants with a combination of the
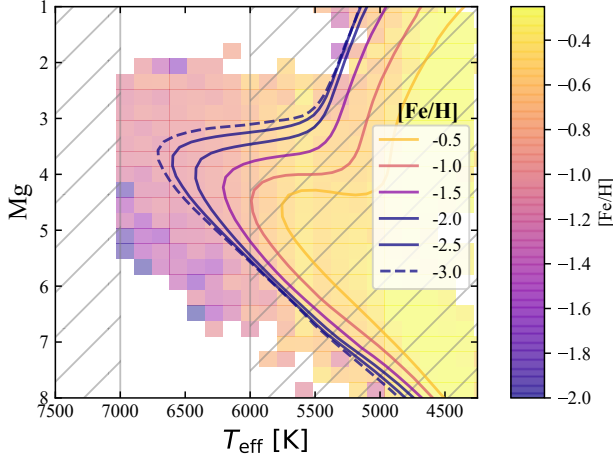
Figure 5. Comparison with the Yonsei-Yale isochrones used for the selection of MSTO stars. The `SPHINX` metallicity estimates are represented by color, where the selection region for MSTO stars, $6000 < T_{\mathrm{eff}}(\mathrm{K}) < 7000$, is denoted by the vertical gray lines.

Canada-France Imaging Survey (Ibata et al. 2017), Pan-STARRS 1, and *Gaia* photometry. We adopt a similar procedure, based on surface-gravity sensitive photometric S-PLUS colors: $(u\mathrm{JAVA} - g\mathrm{SDSS})_0$, $(g\mathrm{SDSS} - r\mathrm{SDSS})_0$, $(J0378 - J0515)_0$, and $(J0660 - J0861)_0$. We train this RFC using dwarf ($N = 3,139$) and giant ($N = 632$) examples, based on the spectroscopic surface-gravity estimates from SEGUE. To address the class imbalance between dwarfs and giants during the training procedure, we implement inverse-frequency class weighting. The dwarf/giant classification probabilities are shown for an independent validation set in Figure 7. The dashed line represents the boundary assigned between dwarf and giant classifications for training. Only stars with $\rho_d > 0.5$ and $\rho_g < 0.5$ are accepted as dwarfs, where ρ_d and ρ_g represent the RFC-assigned likelihood of dwarf and giant classification, respectively. Following the RFC giant rejection, contamination is reduced from $\sim 25\%$ to $\sim 15\%$. We emphasize that this RFC contamination removal preserves the completeness of the sample; only 9% of true dwarf stars are lost following the RFC rejection. Of the 111,815 stars remaining after the SVC mass-selection procedure, 19,735 were rejected by the RFC dwarf-selection procedure. Given the initial giant-contamination estimate of $\sim 25\%$, the estimated total number of remaining giants is $\sim 28,000$, consistent with a final contamination rate of $\sim 10\%$ following RFC rejection. Our final sample of K-type dwarfs comprises 52,035 stars.

5. RESULTS AND DISCUSSION

In this section, we briefly describe the methodology used to study the metallicity and absolute carbon abundance distributions of our MSTO and K-dwarf samples, followed by a presentation and discussion of the results.

5.1. *The MSTO Distribution*

The MSTO sample includes stars that are sufficiently distant ($3 < d$ (kpc) < 9) to comprise stars from the inner- and outer-halo populations, with a likely additional contribution from the thick-disk system. We model the MSTO MDF as the sum of individual Gaussian components, employing Gaussian Mixture Modeling (GMM):

$$\rho(z|\mu_i, \sigma_i) = \sum_{i=1}^{K} \phi_i \mathcal{N}(z, |\mu_i, \sigma_i). \quad (1)$$

Here, we use z to indicate the metallicity, [Fe/H]. Individual Gaussian functions, $\mathcal{N}$, are weighted according to the variable ϕ. We estimate the appropriate weights, central metallicities, μ_i, and scales, σ_i.

5.2. *Reproducing Distribution Families for the K-Dwarf Sample*

The K-dwarf sample from S-PLUS covers a substantially smaller range of distance than the MSTO sample, $1 < d(\mathrm{kpc}) < 6$. Although there are certainly inner- and outer-halo stars represented in the volume we consider, we expect the majority of stars to come from the thick-disk system (including members of both the canonical thick disk and the metal-weak thick disk).

To constrain the shape of the K-dwarf sample MDF, we employ two distinct distribution families: the exponential distribution, and the gamma distribution. Most commonly used to describe the extent of the low-metallicity tail, the exponential probability distribution function can be written as:

$$\rho_e(z|\lambda_e) = N(\lambda_e|z_0, z_f) \cdot e^{-\lambda_e|z|}. \quad (2)$$

The exponential slope is equivalent to $\lambda = \dot{\rho_e}$. Here, z_0 and z_f represent the metallicity limits used for normalization. We include the normalization factor, N, to account for the finite range of the metallicity estimates accessible with our photometric technique:

$$N_*(\boldsymbol{\theta}|z_0, z_f) = \left[\int_{z_0}^{z_f} \rho(z|\boldsymbol{\theta})dz \right]^{-1}. \quad (3)$$

Here, $\boldsymbol{\theta}$ represents the parameters associated with the model. The range over which photometric metallicites are estimated in this work is $-3.5 < [\mathrm{Fe/H}] < 0.0$, although we additionally consider more narrow ranges.
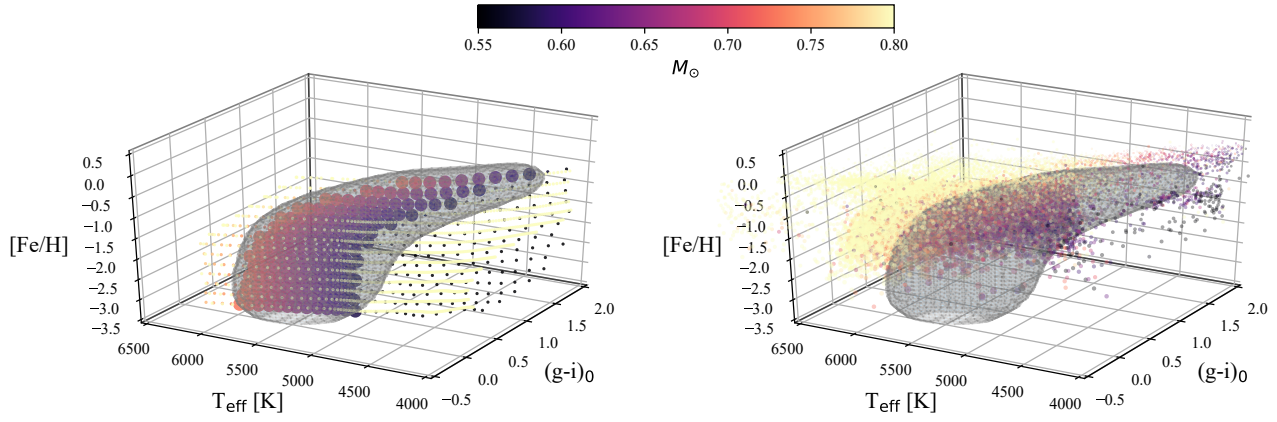
Figure 6. Mass-based selection criteria for the S-PLUS Stripe 82 sample. The left panel shows the stellar isochrones from Demarque et al. (2004), corresponding to the mass range $0.58 < M/M_\odot < 0.75$, color-coded by mass. The resulting SVM decision boundary is shown in the right panel, along with the S-PLUS Stripe 82 sample with `StarHorse`-based mass estimates. The gray region in both plots represents the decision boundary, within which stars are selected. See text for details.
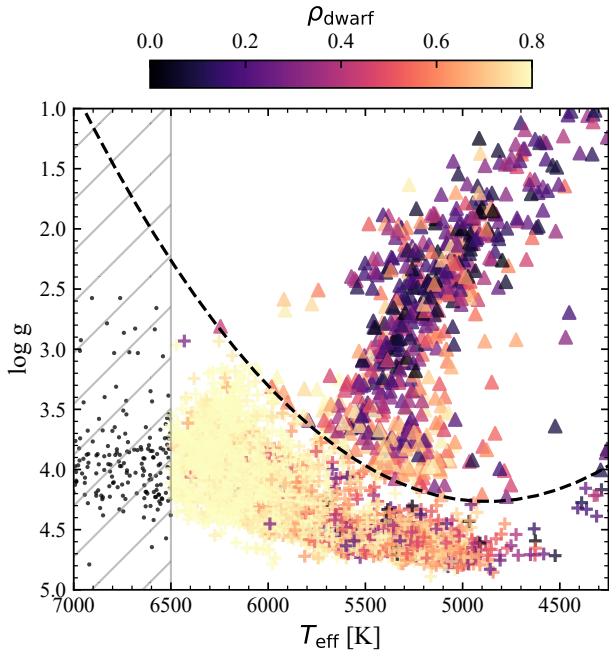

Figure 7. Hertsprung-Russell diagram with surface-gravity classifications from the Random Forest Classifier. Dwarf examples are shown as '+' symbols, and giants as triangles, with the resulting dwarf probabilities represented by color. The dashed line corresponds to the discrimination region between dwarfs and giants used for classification. The dashed region indicates stars beyond the temperature range of the surface-gravity classification, provided for reference nonetheless.

For ease of comparison with similar previous studies, we additionally provide the following form of the exponential distribution:

$$\rho_{10}(z|\lambda_{10}) = N(\lambda_{10}|z_0, z_f) \cdot 10^{-\lambda_{10}|z|}. \tag{4}$$

Note that the exponential slopes are related by a simple change of base: $\lambda_{10} = \lambda_e \log_{10} e$.

In addition, we explore the gamma distribution function. We chose this function for its flexibility in accommodating a diverse range of distribution shapes, and for simplicity in the interpretation of its parameters. The gamma distribution function, ρ_Γ, is:

$$\rho_\Gamma(z|\alpha, \beta) = N_\Gamma(\alpha, \beta|z_0, z_f) \frac{\beta^\alpha}{\Gamma(\alpha)} \cdot |z|^{\alpha-1} e^{-\beta z}. \tag{5}$$

Here, the shape parameter, α, governs the skewness, and the inverse-scale parameter, β, describes the extent of the distribution. We apply an absolute value on the metallicities to transform to the applicable domain $|z| \in (0, \infty)$.

While both forms of the exponential distribution involve the determination of a single parameter, λ, the gamma distribution involves constraining both α and β. Thus, it becomes important to consider the covariance of both parameters. We implement a Bayesian Maximum Likelihood Estimation (MLE) approach in order to estimate the optimal combination of (α, β). Assuming independently sampled data, the model likelihood is simply the product of the individual probabilities:

$$\mathcal{L}(\alpha, \beta) = \prod_i^N \rho_\Gamma(z_i|\alpha, \beta)\rho(\alpha, \beta). \tag{6}$$

All priors are taken to be uniform, and the logarithm of the likelihood is sampled across the posterior space using the `emcee` (Foreman-Mackey et al. 2013) implementation of the Markov Chain Monte Carlo (MCMC; Goodman & Weare 2010) method. As the range of our photometric metallicity sensitivity is limited, we ensure that all PDFs are renormalized according to the range [Fe/H] = [−3.5, −0.5]. The renormalization is itself a function of the model parameters α and β, thus we implement a linear grid interpolation for reference during the MCMC determinations. This grid interpolation samples the values of α and β in increments of 0.01.

Photometric estimates of effective temperature, metallicity, carbonicity, and absolute carbon abundance have been determined for 700,733 stars from the S-PLUS Stripe 82 Data Release 1 with revised calibration, using the Stellar Photometric Index Network Explorer (SPHINX) (Whitten et al. 2019a). As described above, we made two independent selections, a MSTO selection for $6000 < T_{\rm eff}({\rm K}) < 7000$, and a mass-selected K-dwarf sample in the range $0.58 < M/M_\odot < 0.75$. The normalized MDFs and exponential slopes, λ_{10}, are provided in Table 2 for both samples, and we summarize their properties and implications below.

5.3. *MSTO Stars*

The MDF of the MSTO sample is shown in Figure 8, along with the SEGUE spectroscopic sample for comparison. The distributions are limited to the magnitude range of $16.6 < g_0 < 18.3$, corresponding to a distance range of $3 < d({\rm kpc}) < 9$. Note that the apparent mismatch between the MSTO and SEGUE samples above [Fe/H] = −2.0 is expected, due to the metallicity bias in the selection of SEGUE targets, for which we have not corrected here.

The sample is clearly multi-modal, with at least two populations apparent. We address whether the MSTO MDF is better represented by two or three independent populations via application of GMM, indicated by the shaded PDFs in Figure 8. While both models are plausible, a three-component model is determined to be superior on the basis of the Akaiki and Bayesian information criteria (AIC and BIC, respectively), where a difference between models of ΔAIC or ΔBIC > 10 is indicative of a model with significantly higher loss of information (Kass & Raftery 1995). Our three-component Gaussian model produces peaks at [Fe/H] = −0.9, −1.5, and −2.2. The two metal-poor components coincide with the inner and outer halos, respectively (Chiba & Beers 2000; Carollo et al. 2007; Carollo et al. 2010; Beers et al. 2012; Dietz et al. 2020). On the other hand, the metal-rich component is likely a combination of the canonical thick disk

Table 1. Gaussian Mixture Model Components for MSTO Sample

Component	μ[Fe/H]	σ[Fe/H]	ϕ
Two-Component Model			
Comp 1	−1.04	0.35	0.55
Comp 2	−1.96	0.42	0.46
AIC = 8355, BIC = 8387			
Three-Component Model			
Comp 1	−0.89	0.26	0.40
Comp 2	−1.54	0.26	0.36
Comp 3	−2.24	0.33	0.24
AIC = 8261, BIC = 8312			

and the 'splashed disk' (Bonaca et al. 2017; Belokurov et al. 2020), which has the same metallicity as the thick disk, but is extended farther away from the Galactic plane. This interpretation is also supported by the perspective of the local halo stars on the chemo-kinematical space in An & Beers (2020a,b), according to which the local halo samples such as ours are dominated by the above three distinct stellar populations. Their mapping also suggests that the two Gaussian components centered at [Fe/H] = −0.9 and −1.5 are attributed to stars in the so-called red and blue sequences, respectively, in the Hertzsprung-Russell diagram obtained from Gaia DR2 (Gaia Collaboration et al. 2018b; see also Sahlholdt et al. 2019).

Interestingly, we find that the outer-halo population component constitutes as much as 24% of the stars in the MSTO sample, as close as 3 kpc from the Sun. This is consistent with estimates produced by cosmological simulation studies (e.g., Tissera et al. 2014), which suggest an outer-halo contribution of as much as 20–40% in the Solar Neighborhood, based on hydrodynamical modeling (Scannapieco et al. 2009). We describe the Tissera et al. (2012, 2013, 2014) studies further in Section 5.6, in particular the role of accretions and *in situ* star formation.

5.4. *Mass-Selected Local K-Dwarfs*

To select for local K-dwarf stars in the mass range $0.58 < M/M_\odot < 0.75$, we implemented a Support Vector Classification (SVC) scheme using the combination of the broad-band S-PLUS color $(g − i)_0$ and estimates of effective temperature and metallicity obtained from SPHINX. The SVC mass selection was performed on the S-PLUS Stripe 82 sample, with a subsequent RFC giant rejection (see Section 4.3 above), resulting in 52,035 stars with robustly determined metallicity and absolute carbon-abundance estimates within the heliocentric distance $d < 6$ kpc. As this selection constituted a Solar
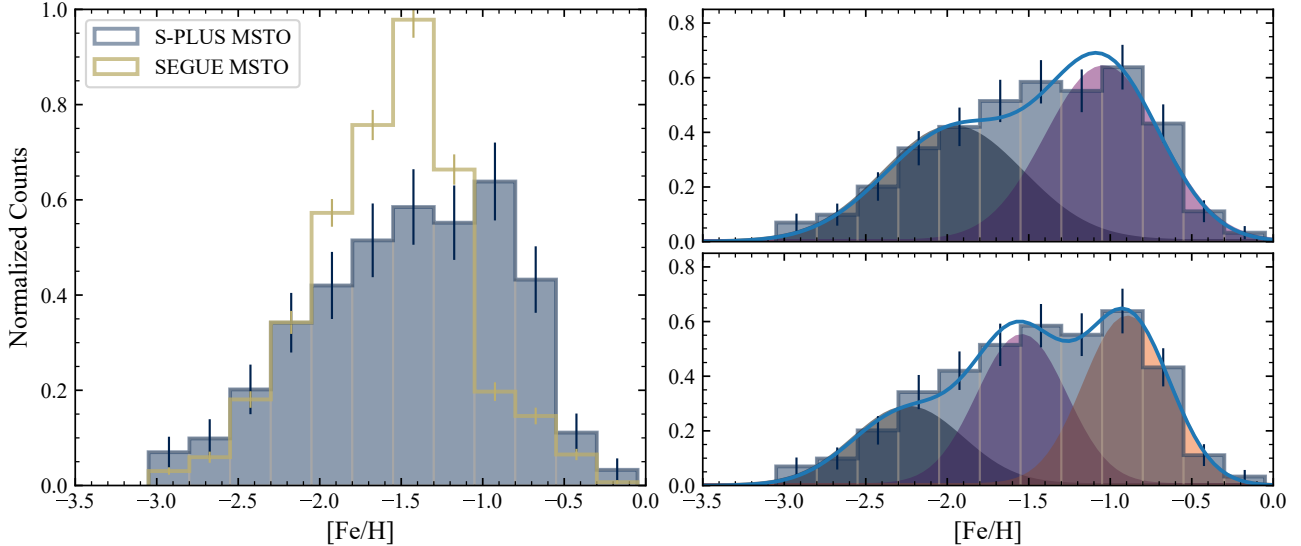
Figure 8. Metallicity distribution function of the S-PLUS and comparison SEGUE MSTO samples. The S-PLUS MSTO sample (*blue histogram*) photometric [Fe/H] distribution is shown in the left panel, along with the SEGUE spectroscopic distribution (*tan open histogram*). The top right panel shows a two-component Gaussian Mixture Model produced for the S-PLUS sample is shown, indicated by the smooth dark blue and purple profiles. The blue line indicates the sum of the model distributions. A three-component Gaussian Mixture Model is shown in the bottom right panel.

Table 2. MDFs for MSTO and K-dwarf Stars

[Fe/H]	MSTO N/N_{tot}	K-dwarf N/N_{tot}	MSTO λ_{10}	K-dwarf λ_{10}
−1.0	0.157	0.323	0.00	0.91
−1.2	0.139	0.214	0.09	0.85
−1.4	0.145	0.146	0.02	0.76
−1.6	0.125	0.107	0.22	0.73
−1.8	0.123	0.074	0.32	0.91
−2.0	0.097	0.043	0.51	1.06
−2.2	0.078	0.028	0.40	0.88
−2.4	0.061	0.020	1.14	0.55
−2.6	0.031	0.016	1.04	0.38
−2.8	0.029	0.014	0.80	0.59
−3.0	0.010	0.009	2.82	1.27

Neighborhood sample, no minimum distance was implemented. A similar selection is made for our SEGUE spectroscopic sample, resulting in 12,337 stars, over heliocentric distances of $1 < d(\mathrm{kpc}) < 6$.

The resulting metallicity and absolute carbon-abundance distributions are shown in Figure 9. The peaks of the [Fe/H] and $A(\mathrm{C})$ distributions are clearly distinct for S-PLUS and SEGUE. The S-PLUS K-dwarf MDF peaks at a higher metallicity, [Fe/H] = −0.64, compared to the SEGUE value of [Fe/H] = −0.81. Similarly, the $A(\mathrm{C})$ distribution of the S-PLUS sample peaks at $A(\mathrm{C}) = 7.85$, compared to $A(\mathrm{C}) = 7.13$ for the SEGUE sample. The largest influence on this separation is likely

the spectroscopic selection function of SEGUE, which is (by design) biased towards low-metallicity stars. For stars of a given [C/Fe], a lower peak [Fe/H] would result in a lower peak $A(\mathrm{C})$, as it is also influenced by the previously known relationship between increasing [C/Fe] with decreasing [Fe/H] (see, e.g., Yoon et al. 2018, and references therein). However, the difference between the peak of the [Fe/H] distributions between the S-PLUS and SEGUE K-dwarf sample of 0.23 dex is not sufficient to account for the $A(\mathrm{C})$ peak separation of 0.54 dex. Given that the K-dwarf selection procedure was implemented identically for both the S-PLUS and SEGUE samples, we conclude that an additional characteristic of the SEGUE selection function is influencing the $A(\mathrm{C})$ distribution, other than the known bias towards low-metallicity stars.

5.4.1. *Comparison of the K-dwarf Metallicity Distributions*

We further explore the shapes of the S-PLUS and SEGUE K-dwarf Stripe 82 MDF in Figure 10. The cumulative distributions of these distributions is shown in the top panel, with the MDF in $\log_{10}(\rho)$ given in the center panel. The value of the exponential slope, as defined in Eqn. 2 and Eqn. 4, is shown as a function of the metallicity in the bottom panel.

The S-PLUS MDF exhibits a steeper profile than the SEGUE profile within the metallicity range $-2.00 < $ [Fe/H] < -1.25, $\lambda_{10} = 0.91 \pm 0.02$ for the S-PLUS sample and $\lambda_{10} = 0.70 \pm 0.02$ for the SEGUE sample. The

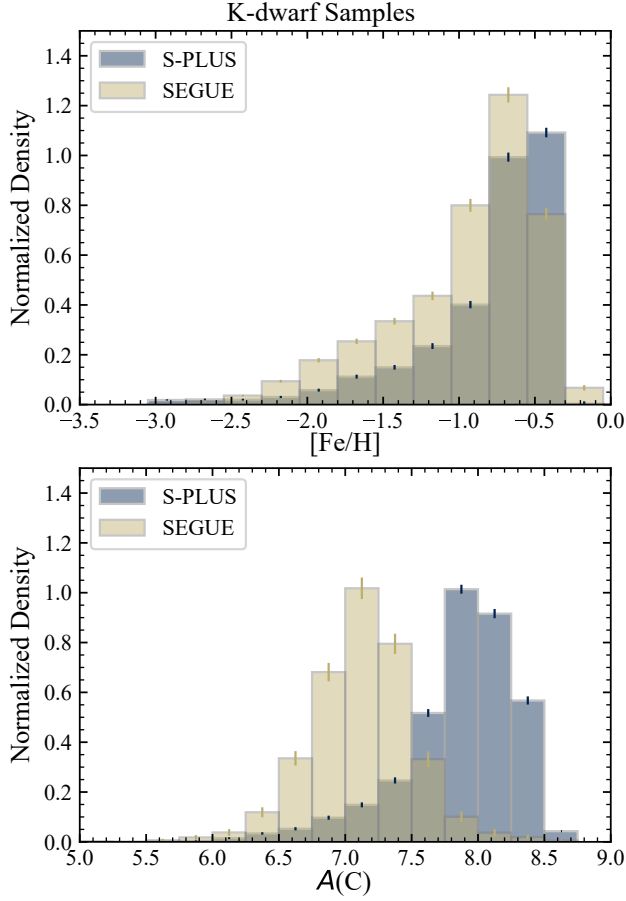**Figure 9.** Metallicity and absolute carbon-abundance distributions of the S-PLUS and SEGUE K-dwarf samples. In the top panel, the [Fe/H] distribution of the S-PLUS sample (*blue*) is shown along with the comparison SEGUE spectroscopic sample (*tan*). Both samples are normalized to their peaks, [Fe/H]= −0.64 and [Fe/H]= −0.81 for the S-PLUS and SEGUE samples, respectively. The corresponding $A(\mathrm{C})$ distribution is shown in the bottom panel. Both distributions are normalized to their peaks, $A(\mathrm{C}) = 7.68$ and $A(\mathrm{C}) = 7.13$ for the S-PLUS and SEGUE samples, respectively.

SEGUE MDF continues to decline steadily below [Fe/H] < −2.0, while the S-PLUS MDF levels off until [Fe/H] < −3.0, beyond which it falls rapidly. The behavior of the exponential slope is depicted in the bottom panel of Figure 10, where the instantaneous value of the slope, λ_{10}, is determined as a function of metallicity.

The SEGUE sample exhibits substantially larger scatter in all parameter estimates for both distributions, most notably the exponential slope of $\sigma(\lambda_e) = 1.06$. These values were determined considering the metallicity range of [Fe/H] = [−2.5, −0.5]. Figure 10 shows, in the top panel, the cumulative frequency distributions of [Fe/H] for the two samples, and in the center panel, the $\log_{10}(\rho)$ of the MDFs. The MDFs in this panel are
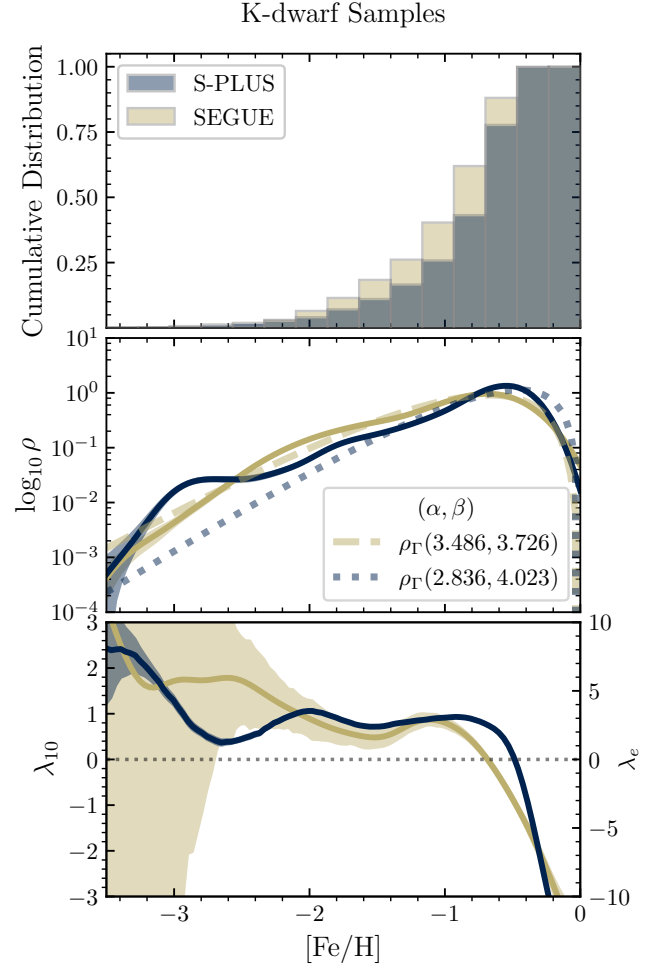
Figure 10. Empirical metallicity distributions of the mass-selected K-dwarf samples from S-PLUS Stripe 82 and SEGUE. In the top panel, the normalized cumulative metallicity distribution is shown for S-PLUS (blue) and SEGUE (tan). The logarithm of the probability distribution is shown in the middle panel, as determined by kernel-density estimation. The gradient of the MDF is shown in the bottom panel as a function of metallicity, with λ_{10} and λ_e given on the left and right of the y-axes, respectively. Uncertainties are determined via successive bootstrap resampling.

determined via kernel-density estimation, averaged over 300 successive bootstrap resamples. To further explore the dependency of the exponential slope on metallicity, we compute the numerical gradient of the MDFs for each sample, shown in the bottom panel. The gradient of $\log_{10}(\rho)$ is seen to vary with metallicity. We note again the significantly smaller uncertainties of λ_{10} for the S-PLUS sample, represented by the shading in this panel, where this uncertainty becomes overwhelming for the SEGUE spectroscopic sample below [Fe/H] = −2.5. Not surprisingly, a one-tail Kolmogorov-Smirnov test re-

jects the null hypothesis that both samples are drawn from the same parent population ($p = 0.01$).

We model the K-dwarf sample MDF with a gamma function, Eqn. 5, using MLE. The resulting posterior distributions of the α and β are listed in Table 3. The uncertainties are reported as the standard deviation of the posterior distributions, and are seen to again be considerably smaller for the S-PLUS sample. This is likely more reflective of the gamma distribution's flexibility and overall ease of determination. To build more representative uncertainties in the most likely values of α and β, we iteratively resample both distributions with bootstrap and successive MCMC determinations. Both samples exhibit similar β values, $\beta = 4.02 \pm 0.03$ and $\beta = 3.73 \pm 0.10$ for the S-PLUS and SEGUE samples, respectively. As this is a two-parameter distribution, and the mean metallicity of both samples is similar, this is not remarkable. However, the optimal values of the shape parameter are markedly different: $\alpha = 2.84 \pm 0.02$ for the S-PLUS sample, and $\alpha = 3.49 \pm 0.08$ for the SEGUE sample. The resulting best-fit gamma distributions are shown in Figure 10.

The gamma distribution is seen to be a more appropriate representation of the metallicity distribution of our K-dwarf sample than an exponential, evidenced by the superior Akaiki and Bayesian Information Criteria in Table 3. The AIC and BIC weigh the maximized likelihood against the model's degrees of freedom. Models with a smaller AIC or BIC are preferred, where $\Delta \mathrm{BIC} > 10$ is considered significant. These values correspond to Fisher-Pearson coefficients of skewness of -1.19 ± 0.01 and -1.0 ± 0.1 for the S-PLUS and SEGUE MDFs, respectively.

While both the S-PLUS and SEGUE MDF slopes are consistent with previous studies, we note that the value of λ_{10} varies significantly across the full metallicity range considered. It is therefore of particular importance to consider the metallicity across which the exponential slope is being considered. At the low metallicity range, $-3.4 < [\mathrm{Fe/H}] < -2.5$, Youakim et al. (2020) reports a slope of 1.0 ± 0.1[8]. We find a similar value at a higher metallicity range, $-1.8 < [\mathrm{Fe/H}] < -1.0$, but find an essentially flat slope around $[\mathrm{Fe/H}] = -2.5$, $\lambda_{10} = 0.1$. Below $[\mathrm{Fe/H}] < -2.75$, the slope increases sharply, reaching $\lambda_{10} = 2.11$ at $[\mathrm{Fe/H}] = -3.0$. This is larger than the slope derived by Da Costa et al. (2019) of 1.5 ± 0.1, who studied a spectroscopic sample of metal-poor giants selected from DR 1.1 of the SkyMapper survey. Nevertheless,

---

[8] The value reported as $\Delta(\log \mathrm{N})/\Delta[\mathrm{Fe/H}]$ in the Youakim et al. (2020) study is equivalent to the λ_{10} used in this work.

our result supports the conclusion that the MDF drops more steeply at the lowest metallicity. We do not attribute the rapid increase in the slope seen in Figure 10 to the size of our sample. Below $[\mathrm{Fe/H}] < -2.75$, we have 467 candidates, with 61 stars below $[\mathrm{Fe/H}] < -3.0$.

5.5. Comparison with Previous Work

Figure 11 shows a comparison of our MDF results with those from the studies of An et al. (2015) and Youakim et al. (2020), and considered in more detail below.

5.5.1. Comparison with An et al. (2013, 2015)

As described in § 4.3, we made a mass-based selection for the K-dwarf sample for a number of reasons. One of the advantages of such a selection is that we can reduce bias against metallicity, which is normally inherent to color- or T_{eff}-based selections due to a strong correlation between metallicity and T_{eff}. An et al. (2013, 2015) also made such attempts to construct in situ halo samples of main-sequence dwarfs in Stripe 82. Their selection, based on stellar masses in the range $0.65 < M/M_{\odot} < 0.75$, includes approximately $2,500$ sources in each of three photometric catalogs, which have been independently generated from multiple SDSS imaging data.

The top panels of Figure 11 show a comparison of the normalized MDFs from the S-PLUS K-dwarf sample (purple solid line) with that in An et al. (2015, red triangles). While the S-PLUS K-dwarf sample is steeply rising towards higher metallicities, the An et al. (2015) MDF levels off at $[\mathrm{Fe/H}] \sim -1.5$. The large discrepancy at higher metallicities originates from important differences in the detailed sample selections in these two studies. The An et al. (2013, 2015) samples are strictly limited to sources at $5 < d \lesssim 10$ kpc with $|b| > 35°$. On the other hand, the S-PLUS sample includes more local stars in the thick disk ($d > 1$ kpc), resulting in a factor of ten larger sample size, and more importantly, leading to a skewed MDF by including significantly more metal-rich disk (and metal-weak thick disk) stars.

Nonetheless, at $[\mathrm{Fe/H}] < -1.7$, where the contributions from metal-rich disk stars are minimal, the observed shape of the MDF from the S-PLUS K-dwarf sample is similar to that of An et al. (2015), considering the size of the errors from both studies. Interestingly, the latter MDF agrees better with that of the S-PLUS MSTO sample (purple dotted line), at least up to $[\mathrm{Fe/H}] \sim -1.3$. An et al. (2013, 2015) judged that their MDF is complete at $[\mathrm{Fe/H}] < -1.2$, above which the number of metal-rich stars are under-estimated at large distances, because more metal-rich stars in a given mass bin become fainter, and therefore are under-populated in a magnitude-limited sample. The metallicity bias for the metal-poor star samples were mitigated in their

Table 3. Maximum Likelihood Parameter Estimates for K-dwarf Sample Metallicity Distributions

	Exponential Distribution (ρ_e)					
Sample	λ_{10}	$\sigma(\lambda_{10})$	λ_e	$\sigma(\lambda_e)$	AIC	BIC
S-PLUS	0.85	0.26	1.95	0.59	31144	31153
SEGUE	0.70	0.46	1.62	1.06	14559	14566
	Gamma Distribution (ρ_Γ)					
Sample	α	$\sigma(\alpha)$	β	$\sigma(\beta)$	AIC	BIC
S-PLUS	2.84	0.02	4.02	0.03	**28505**	28523
SEGUE	3.49	0.08	3.73	0.10	**12577**	12591

studies by adopting detailed mass-metallicity-distance cuts.[9] Therefore, the agreement between the MSTO sample and An et al. (2015) at [Fe/H] $\lesssim -1.2$ is reassuring, given the fact that they are based on different imaging data and independent metallicity estimators.

When decomposed into a two-component Gaussian model, An et al. (2013, 2015) found peaks at [Fe/H] = -1.5 ± 0.2 and [Fe/H] = -2.1 ± 0.2 for the inner- and outer-halo components, respectively, taken as an average from the three photometric catalogs employed in their studies. These peak values are in good agreement with the peaks identified from the three-component Gaussian decomposition of our MSTO sample (Table 2); the metal-rich component centered at [Fe/H] = -0.9 can be attributed to the thick-disk and metal-weak thick disk stars in the MSTO sample with $d > 3$ kpc, which are not present in An et al. (2013, 2015). We also find that the fraction of the low-metallicity halo component from the MSTO sample (24%) is compatible with the ~ 20–35% in An et al. (2013), although it is smaller than the ~ 35–55% reported in An et al. (2015).

5.5.2. *Comparison with Youakim et al. (2020)*

We now compare our MSTO sample with the Youakim et al. (2020) study of MSTO stars from the *Pristine* survey (Starkenburg et al. 2017). Note that the Youakim et al. (2020) selection covered a larger footprint than our S-PLUS sample, some $2,500\,\mathrm{deg}^2$, predominately above the Galactic plane, with $|b| > 20°$, although it included SDSS Stripe 82. Their selection also extends to larger heliocentric distances, $6 < d$ (kpc) < 20, as compared with our MSTO sample range of $3 < d$ (kpc) < 9. Similar to An et al. (2015), the Youakim et al. (2020) photometric methodology becomes unreliable for metallicities above [Fe/H] > -1.5. For our MSTO sample, we do not expect such bias until [Fe/H] > -0.75.

Similar to our MSTO selection, the *Pristine* selection suggests the presence of three populations, with peak metallicities corresponding to [Fe/H] = $-1.32, -1.89$, and -2.45. The most metal-poor component is in general agreement with the value determined for our MSTO selection (see Table 1), [Fe/H] = -2.51, although our fraction of this population, 27%, is somewhat smaller than determined for the *Pristine* sample, 33%. This is likely due to the larger contribution from thick-disk system stars to our MSTO sample, based on $d > 3\,\mathrm{kpc}$.

5.6. *Comparison with the Aquarius Simulation Aq-C-5 of Tissera et al.*

Over the past decade, cosmologically based numerical simulations of the formation and evolution of Milky-Way-size systems have grown in sophistication to the point that insight into the chemical-evolution history of our galaxy can be gained by comparison with observations such as ours.

Among these simulation studies is the Aquarius project, originally presented in Scannapieco et al. (2009). This high-resolution hydrodynamical simulation was produced with a modified version of GADGET-3 (Scannapieco et al. 2005, 2006) as part of the Aquarius Project of the Virgo Consortium (Springel et al. 2008), and explicitly models the chemical evolution of the baryons via contributions from Type II and Type Ia supernovae. We refer the interested reader to Scannapieco et al. (2009) for a detailed discussion of the chemical modeling, and focus our attention on one of the MW-mass halos studied by Tissera et al. (2013, 2014). In Tissera et al. (2013), a simple binding-energy criteria was developed to separate the halo component of the Aquarius MW-mass galaxies into an inner-halo population (IHP) and and outer-halo population (OHP). By tracking contributions of stars formed both within and outside of the main progenitor's virial radius, Tissera et al. (2014) highlighted the contrasting roles of accretion and *in situ* star formation in the evolution of MW-mass halos, and most importantly, the influence of these two mechanisms on the resulting chemo-dynamical distributions.

---

[9] The same sample cut was not applied to the S-PLUS K-dwarf sample in this exploratory study, in order to maximize the number of metal-poor stars in the carbonicity estimation (see below).
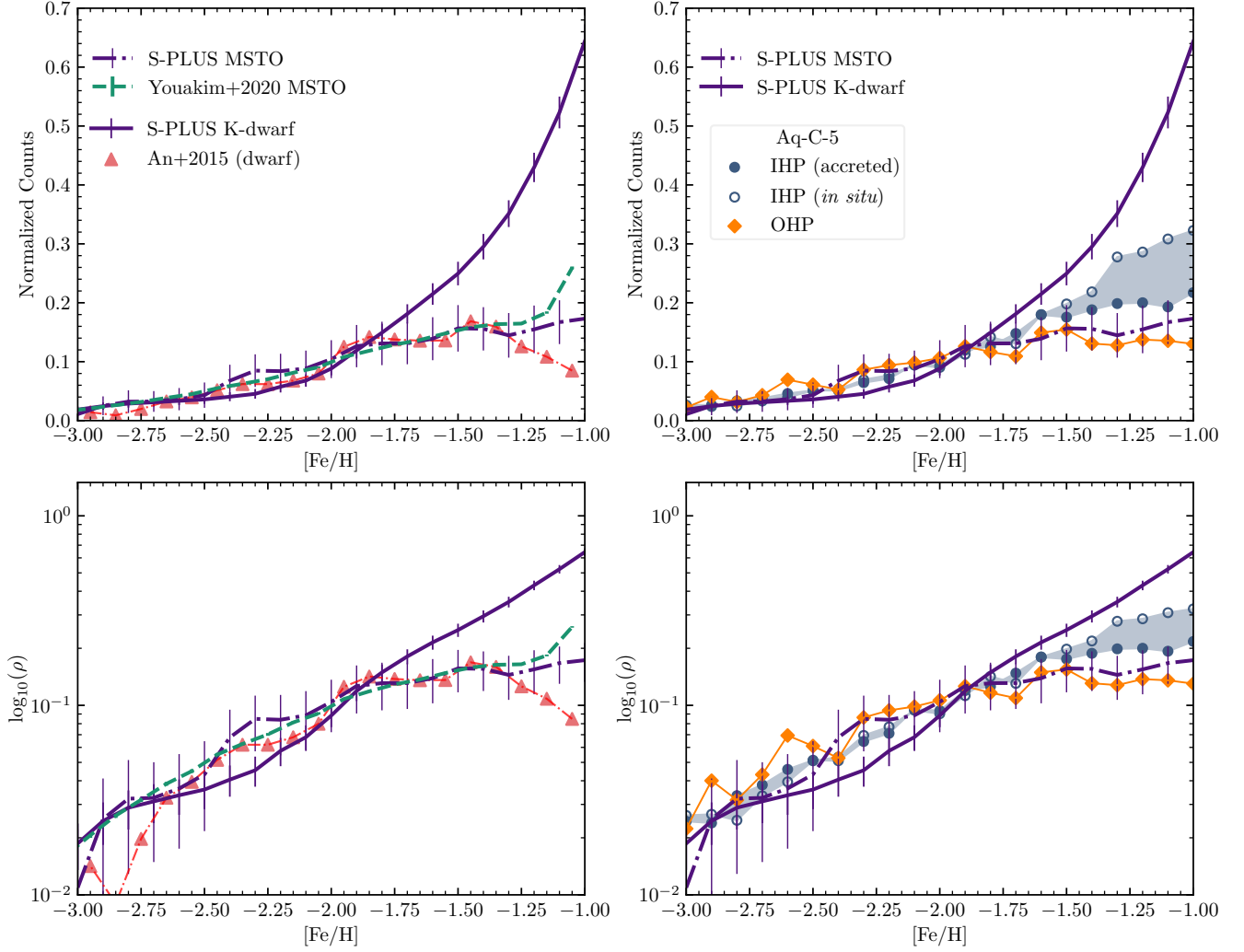
Figure 11. Metallicity distribution functions of the S-PLUS MSTO (*purple, dotted*) and K-dwarf (*purple, solid*) samples compared with literature studies. In the left panel, the observational studies from An et al. (2015) (*red, triangles*) and Youakim et al. (2020) (*green, dashed*) are shown in comparison to the S-PLUS samples. (*Right:*) Simulation results for the inner-halo population (IHP; *dark-blue circles*) and outer-halo population (OHP; *orange diamonds*) of the `Aq-C-5` Tissera et al. (2014) halo sample are shown for comparison. The IHP of `Aq-C-5` is further divided into the accreted (*filled points*) and *in situ* (*hollow points*) components. The shading indicates the region where we expect MDFs composed of contributions from both components (see text for details). The logarithm of each distribution is shown in the bottom panels. All distributions are normalized to the interval [Fe/H] = [−2.0, −1.5] for comparison.

We compare our observations with a particular halo from Aquarius, referred to as `Aq-C-5`. Of the eight MW-mass halos produced in Aquarius, `Aq-C-5` was determined to be the most similar to the MW halo population, on the basis of metallicity and age-distribution studies from Carollo et al. (2018) and Whitten et al. (2019b), the chemo-dynamical properties of the old population in the central regions (Tissera et al. 2018), and the [α/Fe] radial profiles in the inner region (Fernández-

Alvar et al. 2019). We restrict our analysis to the portion of the stellar halo of `Aq-C-5` with heliocentric distances in the range 3 < d(kpc) < 9. MDFs determined for the `Aq-C-5` halo were weighted according to the particle mass, as these particles represent conglomerates of stars. In the right panels of Figure 11, we consider the MDFs of `Aq-C-5` halo, which includes the OHP, and *in situ* and accreted components of the IHP. Here, the IHP is indicated by light-blue circles; the OHP is shown in orange.

Shading indicates the transition between the accreted and *in situ* components of the IHP, or in other words, the region we expect to be occupied by MDFs composed of contributions from the two extremes of halo formation, namely pure accretion or pure *in situ* star formation.

Across the metallicity range $-2.5 < [\text{Fe/H}] < -1.5$, the MDF of the S-PLUS MSTO sample is consistent with the `Aq-C-5` IHPs. Above $[\text{Fe/H}] = -1.50$, the MDF of the S-PLUS MSTO sample is more consistent with the OHP, although we acknowledge the limitations of this comparison, and do not suggest that the MSTO sample is dominated by outer-halo stars at $[\text{Fe/H}] > -1.50$. Below $[\text{Fe/H}] = -2.5$, the increase in stars noted in the S-PLUS MSTO MDF is also seen in the MDF of the OHP of `Aq-C-5`.

Similar to the S-PLUS MSTO sample, the S-PLUS K-dwarf sample MDF is consistent with the IHP of `Aq-C-5` within the range $-2.5 < [\text{Fe/H}] < -1.5$. At $[\text{Fe/H}] > -1.5$, however, the S-PLUS K-dwarf sample greatly exceeds both the inner- and outer-halo populations of `Aq-C-5`. We note that the `Aq-C-5` stellar halos do not include stars with circularity $(J_z/J_{z,\max(E)})$ larger than 0.65 (see Tissera et al. 2013, for details), effectively removing the disk population that is known to dominate the S-PLUS K-dwarf sample. This limits the extent to which comparisons between the S-PLUS K-dwarf sample and `Aq-C-5` can be made at higher metallicities, where the disk system is expected to dominate. Below $[\text{Fe/H}] = -2.0$, however, this complication is minimal, and we see that the K-dwarf MDF is somewhat steeper than both the inner- and outer-halo populations.

It is clear that future refinements of the photometric MDFs, such as ours, can help constrain the stellar contributions from the accreted and *in situ* populations predicted by such simulations. Interestingly, it is the regime of the MDF at higher-metallicity, $[\text{Fe/H}] > -1.50$, which exhibits the largest contrast between accreted and *in situ* populations, and is thus of particular importance to constrain their respective roles.

5.7. *Photometric Absolute Carbon Abundance*

Estimates of absolute carbon abundance, $A(\text{C})$ (and $[\text{C/Fe}]$), are obtained for the S-PLUS K-dwarf sample, resulting in robust determinations for $51,003$ stars across the carbon abundance range $5.0 < A(\text{C}) < 8.5$. Figure 12 shows $A(\text{C})$ vs. $[\text{Fe/H}]$, following Yoon et al. (2016). Here, the color-coding indicates the logarithmic number density, determined from a 2-D kernel-density estimate with a standard deviation assigned to the typical estimated uncertainty in $A(\text{C})$, ~ 0.35 dex. The dashed line corresponds to $[\text{C/Fe}] = +0.7$, the level of carbonicity used to separate CEMP stars from carbon-normal stars. This diagram also indicates the approximate location of the morphological Group I, Group II, and Group III stars suggested by Yoon et al. (2016), although our inability to estimate $[\text{Fe/H}]$ for stars below $[\text{Fe/H}] = -3.5$ limits the number of lower-metallicity Group II and Group III stars we can identify.

A total of 364 stars populate the CEMP region above $[\text{C/Fe}] = +0.7$. Excepting the small number of possible Group III stars, two distinct clusters are apparent among the CEMP stars, roughly consistent with the morphology identified by Yoon et al. (2016), namely a large grouping of stars $-2.5 < [\text{Fe/H}] < -1.0$ and $7.5 < A(\text{C}) < 8.5$, and a separate population at $-3.5 < [\text{Fe/H}] < -2.0$ and $6.0 < A(\text{C}) < 7.25$. We model these clusters using a K-means approach, for which we determine cluster centers at $([\text{Fe/H}], A(\text{C})) = (-1.6, 8.0)$ and $([\text{Fe/H}], A(\text{C})) = (-2.8, 6.5)$, respectively. These clusters are represented in Figure 12 by the red circle and cross, respectively. The stars associated with the higher-metallicity cluster constitute $\sim 70\%$ of the CEMP stars in our dwarf sample.

Yoon et al. (2016) identified similar populations in $A(\text{C})$ vs. $[\text{Fe/H}]$, produced from a compilation of high-resolution spectroscopic determinations, which was built upon the literature compilation of Placco et al. (2014). The peak at $A(\text{C}) \sim 8.0$ in Yoon et al. (2016), designated as Group I, was found to constitute the majority of CEMP-s and CEMP-r/s stars[10] stars, while a lower peak at $A(\text{C}) \sim 6.3$, designated Group II, was found to possess a majority of CEMP-no stars. This diversification is a compelling distinction, with implications on the first-generation star progenitors required to produce the observed CEMP star behavior. We note that a third population, Group III, is located at lower metallicity, $[\text{Fe/H}] < -3.0$, and centered on $A(\text{C}) \sim 6.8$. Group III CEMP stars are also predominantly CEMP-no stars, and are perhaps the most interesting with regards to the impact on the origin of carbon. However, as noted above, Group III stars with $[\text{Fe/H}] < -3.5$ are effectively inaccessible with the current limitations of the photometric metallicity technique central to this work.

For these reasons, we identify the clusters identified by our K-means method as the Group I and Group II populations discussed in Yoon et al. (2016), and suggest that the handful of stars seen in Figure 12 at lower metallicities, $[\text{Fe/H}] < -2.5$, and $A(\text{C}) \sim 7.0 - 7.5$ may be Group III CEMP stars in the S-PLUS K-dwarf sample.

---

[10] CEMP-s: $[\text{C/Fe}] > +0.7$, $[\text{Ba/Fe}] > +1.0$, and $[\text{Ba/Eu}] > +0.5$
CEMP-r/s: $[\text{C/Fe}] > +0.7$ and $0.0 < [\text{Ba/Eu}] < +0.5$
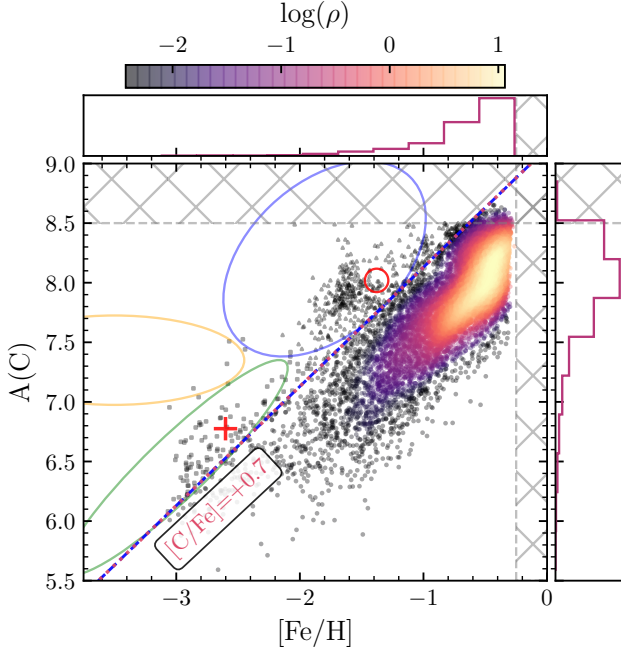CEMP-no : $[\text{C/Fe}] > +0.7$ and $[\text{Ba/Fe}] < 0.0$

Figure 12. [Fe/H] vs. A(C) distribution of the S-PLUS Stripe 82 K-dwarf sample. The number density (ρ) is determined by kernel-density estimation and represented by the color-coding shown. The line corresponding to [C/Fe] = +0.7 indicates the adopted boundary for carbon-enhanced stars, with two populations clearly present in the CEMP region. The red cross and circle markers at ([Fe/H], A(C)) = $(-2.8, 6.5), (-1.6, 8.0)$ represent the cluster centers determined by K-means clustering. Ellipses corresponding approximately to the CEMP Group I (*blue*), II (*green*), and III (*orange*) identified in Yoon et al. (2016) are shown for reference.

5.7.1. *Cumulative CEMP Fraction Comparison*

The overall frequency of CEMP stars in our K-dwarf sample is 1.6%, and increases rapidly at lower metallicity. Nearly half, 48%, of all stars in our sample below [Fe/H] < −2.5 are CEMP stars. Of the 14 stars below [Fe/H] < −3.0, 14 (78%) are CEMP stars. We compare this result with with two studies from the literature, Yoon et al. (2018) and Placco et al. (2014). First, the Yoon et al. (2018) study explored the spatial distributions of [C/Fe] and [Fe/H] with medium-resolution ($R \sim 1,300$) spectroscopy from the AAOmega Evolution of Galactic Structure; AEGIS) survey. This study conveniently includes regions of the Southern Galactic Hemisphere, permitting comparisons with Stripe 82. However, the Yoon et al. (2018) study was concerned with sub-giants and giants, thus probing the CEMP fraction at considerably larger heliocentric distances than the S-PLUS K-dwarf sample. The Placco et al. (2014) study obtains the CEMP fraction based on a compilation of the high-resolution spectroscopy available at the

time, from the SAGA database (Suda et al. 2008) and the literature compilation of Frebel et al. (2010). This sample also includes a large fraction of giants, as well as stars with high effective temperatures (T_{eff} > 6000 K), and thus a similar caution is given with regards to the extent with which comparisons can be made. We refer to Table 1 of Placco et al. (2014), which consists of the cumulative CEMP and CEMP-no fractions produced from the 505 stars below [Fe/H] < −2.0 with high-resolution spectroscopy.

Figure 13 compares the cumulative CEMP fraction of our K-dwarf sample with those from Yoon et al. (2018) and Placco et al. (2014). For the K-dwarf CEMP and CEMP-no fractions, the shaded area represents the uncertainties estimated from the binomial proportion confidence interval (see Wilson 1927, for details). In the left panel of Figure 13, we see that the S-PLUS K-dwarf cumulative CEMP fraction is fairly consistent with the estimates from Yoon et al. (2018). While the K-dwarf CEMP fraction at [Fe/H] ≤ −1.5 of 20% is in excess of the Yoon et al. (2018) estimate of 14%, both studies indicate a CEMP fraction above 60% at metallicities below [Fe/H] = −3.0. In the right panel of Figure 13, we see a larger contrast between the CEMP fraction from the S-PLUS K-dwarf sample with the Placco et al. (2014) study. While the CEMP fraction at [Fe/H] ≤ −2.0 of the S-PLUS K-dwarf sample, ∼ 27%, is consistent with the Placco et al. (2014) value of 33%, the S-PLUS K-dwarf sample rises faster at lower metallicities, somewhat exceeding the Placco et al. (2014) estimate at [Fe/H]≤ −3.0.

The sub-class of CEMP stars that exhibit no over-abundances of neutron-capture elements, the CEMP-no stars (Beers & Christlieb 2005), are of particular interest. The carbon enhancements in CEMP-no stars are thought to arise from *intrinsic* processes (Yoon et al. 2016), such as pollution of their natal gas by massive stars, rather than from *extrinsic* mass-transfer events from an evolved companion in binary systems (Hansen et al. 2016). These stars are therefore believed to be true second-generation stars, with chemical characteristics reflecting the elemental signatures produced by first-generation massive stars. While confirmation of CEMP-no stars conventionally requires determination of the barium abundance, [Ba/Fe], Yoon et al. (2016) demonstrated that CEMP-no stars can be confidently discriminated from CEMP-s and CEMP-r/s stars by their locations on the Yoon-Beers diagram. Following the prescription from Lee et al. (2017) and Placco et al. (2018), we select stars with A(C) < 7.5, and consider the resulting cumulative CEMP-no fraction in Figure 13.
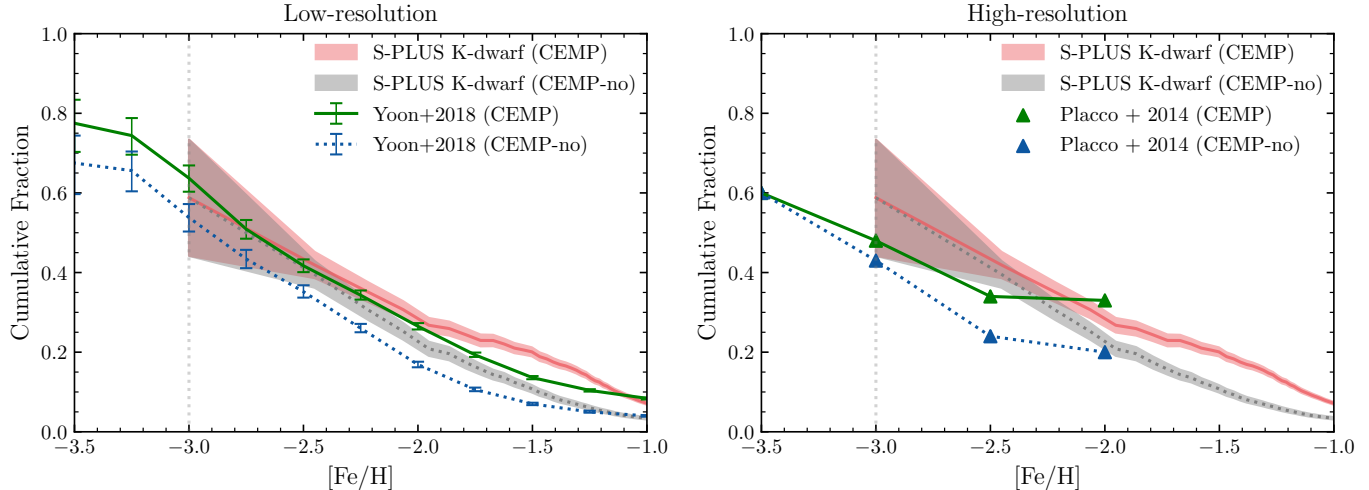
Figure 13. Cumulative CEMP-star fractions for the S-PLUS K-dwarf sample compared with literature studies. In the left panel, the S-PLUS K-dwarf cumulative CEMP-star fraction (*red, shaded*) and CEMP-no star fraction is shown along with the Yoon et al. (2018) study produced with medium-resolution spectroscopy from AEGIS. The Placco et al. (2014) study produced with high-resolution spectroscopy is shown in the right panel. Shading on the K-dwarf CEMP and CEMP-no frequencies represents the binomial confidence intervals, averaged by successive bootstraping. The dotted vertical line represents the current limit of this work, below which the number of stars is insufficient.

.

While qualitatively similar, the crude estimate of the cumulative CEMP-no fraction for the S-PLUS K-dwarf sample consistently exceeds the medium-resolution spectroscopic result from Yoon et al. (2018) by a small amount, $\sim 5\%$ at metallicities below [Fe/H< -1.5. The difference is even larger when compared with the high-resolution spectroscopic estimate from Placco et al. (2014), by as much as $\sim 20\%$. However, both the S-PLUS K-dwarf sample and the Placco et al. (2014) result indicate equivalent cumulative CEMP and CEMP-no fractions at [Fe/H] < -3.0, suggesting that the great majority of CEMP stars below [Fe/H]$= -3.0$ belong to the CEMP-no class.

The cumulative CEMP fraction produced in this work is generally in best agreement with the medium-resolution result from Yoon et al. (2018), supporting the conclusion that photometric techniques such as those discussed in this work are a valid means of probing the CEMP fraction of MW stars. As explored in Yoon et al. (2020), the strength of carbon molecular bands in the visible spectrum can become highly disruptive to low- and medium-resolution spectroscopic studies, where determination of the proper pseudo-continuum is both crucial and difficult. This has the effect of limiting the range of CEMP stars that can be studied at these resolutions by means of the CH G-band, effectively to $A(C) < 8.5$ (Yoon et al. 2020). Stars in excess of this $A(C)$ value are therefore excluded from estimates of the CEMP fraction. It is not clear what effect this has on the frequencies reported from such studies. While

estimates of $A(C)$ produced with high-resolution spectroscopy are largely immune to the difficulties imposed on pseudo-continuum determination, studies like Placco et al. (2014) are nevertheless challenged by the significantly smaller numbers of stars with available high-resolution spectra. Interestingly, the number of stars in the S-PLUS K-dwarf sample with [Fe/H] < -2.0, 513, is about the same as the 502 stars from (Placco et al. 2014), which represent nearly all VMP stars with high-resolution carbon measurements available at the time of publication. It is clear that future data releases from S-PLUS will provide substantially larger samples of metal-poor stars with which to further constrain the CEMP fraction in the MW.

5.8. *Catastrophic Failures of Photometric Metallicity Estimates*

Common to all techniques of photometric-metallicity estimation is the extreme sensitivity to errors in the adopted metallicity indicator, whether a filter magnitude or colors, in particular at very low metallicities or high temperatures, where the metallicity dependence of the photometry is diminished. This sensitivity introduces the possibility of "catastrophic failure", which we define as gross errors by the adopted metallicity estimator(s) of $|\Delta[Fe/H]| > 1.0$ dex. While the neural-network approach employed in this work is not immune to the occurrence of catastrophic failure, a number of measures have been taken to mitigate this problem. The

concensus ANN procedure we have adopted considered the ensemble of networks contributing to the final estimates, weighing each by its validation score achieved during training. Each network is trained on a unique combination of photometric colors, minimizing the influence of any single color on the final estimate. Finally, each network performs an interpolation check during estimation, flagging estimates from inputs outside the parameter space seen during training. This, along with the use of multiple metallicity indicators, results in a very low rate of catastrophic errors for our photometric metallicity estimates, when compared with external spectroscopic estimates: for metallicities below [Fe/H] < −2.0, ∼ 0.4% for |Δ[Fe/H]| > 1.0 dex, and only 6% for |Δ[Fe/H]| > 0.50 dex.

The *Pristine* survey has proven quite successful with respect to candidate metal-poor star detection, with success rates for the identification of bona-fide [Fe/H] < −2.5 stars of 56% (Aguado et al. 2019). The *Pristine* survey exhibits catastrophic failure rates of 1.3% for |Δ[Fe/H]| > 1.0 dex, and 9.3% for |Δ[Fe/H]| > 0.50 dex for stars with [Fe/H] < −2.0, when compared with an overlapping sample of SDSS and SDSS/SEGUE stars (calculations based on data from Starkenburg et al. 2017). We emphasize the *substantial decrease in the catastrophic-failure rates* seen in this study to highlight the advantage of narrow-band photometry (in particular with multiple metallicity-sensitive filters), in conjunction with the sophistication of machine-learning techniques, in this case SPHINX, compared with traditional (often simple polynomial-based) photometric techniques used by many previous efforts. Given the quite low catastrophic-failure rates that are achievable, our photometric approach would appear capable of precision studies of the MDFs of stellar populations without the need for time-consuming medium- or high-resolution spectroscopic follow-up, except perhaps at the very lowest metallicities, e.g., [Fe/H] ≤ −3.0.

6. CONCLUSIONS

Photometric estimates of effective temperature, T_{eff}, metallicity, [Fe/H], carbonicity, [C/Fe], and absolute carbon abundances, $A(\mathrm{C})$, are produced using the novel artificial neural network methodology SPHINX, taking advantage of the mixed-bandwidth photometry obtained by the Southern Photometric Local Universe Survey (S-PLUS). Two selections are made from the Stripe 82 data release from S-PLUS, a main-sequence turnoff (MSTO) sample of the inner/outer halo and thick-disk populations ($N = 771$), and a main-sequence K-dwarf sample ($N = 52,035$), selected based on stellar mass. We study the MDFs for both samples, and conduct an additional exploration of the $A(\mathrm{C})$ distribution of our mass-selected K-dwarf sample.

We reproduce the MDF of the halo with our MSTO sample, with peaks in the distribution corresponding to previously understood populations. From the mass-selected K-dwarf sample, we produce the first photometric $A(\mathrm{C})$ vs. [Fe/H] diagram of the Solar Neighborhood ($1 < d(\mathrm{kpc}) < 6$). We constrain the exponential slope of the local-volume MDF, produced with K-dwarf stars, but find significant variation in the value, $\lambda_{10,[\mathrm{Fe/H}]} = 0.9 \pm 0.2$, across the metallicity range considered in this work (which is well-constrained down to [Fe/H] = −2.75). Our results suggest that the Solar Neighborhood MDF is better represented by a gamma distribution.

We identify 364 CEMP candidates for follow-up spectroscopic analyses, as well as provide compelling evidence supporting the diverse CEMP morphology discussed in Yoon et al. (2016). We find fractions of carbon enhancements similar to previous spectroscopic studies, highlighting S-PLUS as a useful probe of the characteristics of CEMP stars in the MW. Our results confirm that as many as 60% of extremely metal-poor stars (EMP; [Fe/H] < −3.0) are CEMP-no stars.

While photometric surveys are an ideal means with which to identify candidate metal-poor stars for high-resolution spectrscopic follow-up, the typical magnitude ranges of such surveys (e.g., SDSS with $14.0 < g < 22$) present challenges, as faint targets ($g > 15$) require long integration times with even 6.5-10 meter class telescopes (Mendes de Oliveira et al. 2019). For this reason, we anticipate the component of S-PLUS known as the Ultra-Short Survey (USS), that will cover the same footprint as the main survey of S-PLUS with exposure times that are 1/12th of main survey. The USS will enable identification of metal-poor candidates as bright as 8th mag in the broad-band filters, compared with 12th mag for the main survey (see Mendes de Oliveira et al. 2019, for details). In addition to the effectiveness demonstrated in this work of stellar chemical-abundance determinations with S-PLUS, the USS thereby positions S-PLUS as a crucial component for the future of bright metal-poor star studies in the Solar Neighborhood.

The constraints on the metallicity distribution functions of the inner-halo region and Solar Neighborhood produced in this work present a crucial means with which to constrain cosmological models of Milky Way formation and chemical evolution, while circumventing many of the known biases inherent to spectroscopic methods. In particular, we demonstrate the potential to discern the complementary roles of accretion and *in situ* star formation in the chemical evolution of the

Milky Way. We expect that robust photometric carbon abundance determinations will play an increasingly important role in the differentiation between cosmological models of Galactic chemical evolution, particularly by more tightly constraining the CEMP and CEMP-no fractions of the inner/outer halo regions and the Solar Neighborhood.

Stellar chemical-abundance determinations with narrow-band photometric surveys like J-PLUS and S-PLUS are a natural application of machine learning algorithms like `SPHINX`, described in Whitten et al. (2019a) and implemented in this work. `SPHINX` has been shown to produce robust estimates of effective temperature, metallicity, carbonicity, and absolute carbon abundance in stars, with a remarkably low rate of catastrophic failure. We anticipate the utility of `SPHINX` (or similar approaches) for future data releases from J-PLUS and S-PLUS, in particular because several of the narrow-band filters in these efforts will soon be calibrated to enable estimation of additional valuable elemental abundances, such as the α-elements Mg and Ca.

REFERENCES

Abazajian, K. N., Adelman-McCarthy, J. K., Agüeros, M. A., et al. 2009, ApJS, 182, 543, doi: 10.1088/0067-0049/182/2/543

Aguado, D. S., Youakim, K., González Hernández, J. I., et al. 2019, MNRAS, 490, 2241, doi: 10.1093/mnras/stz2643

Allende Prieto, C., Beers, T. C., Wilhelm, R., et al. 2006, ApJ, 636, 804, doi: 10.1086/498131

An, D., & Beers, T. C. 2020a, ApJ, 897, 39, doi: 10.3847/1538-4357/ab8d39

—. 2020b, arXiv e-prints, arXiv:2011.10740. https://arxiv.org/abs/2011.10740

An, D., Beers, T. C., Santucci, R. M., et al. 2015, ApJL, 813, L28, doi: 10.1088/2041-8205/813/2/L28

An, D., Beers, T. C., Johnson, J. A., et al. 2013, ApJ, 763, 65, doi: 10.1088/0004-637X/763/1/65

Anders, Khalatyan, A., Chiappini, C., et al. 2019, A&A, doi: 10.1051/0004-6361/201935765

Anthony-Twarog, B. J., Laird, J. B., Payne, D., & Twarog, B. A. 1991, AJ, 101, 1902, doi: 10.1086/115815

Anthony-Twarog, B. J., Sarajedini, A., Twarog, B. A., & Beers, T. C. 2000, AJ, 119, 2882, doi: 10.1086/301407

Asplund, M., Grevesse, N., Sauval, A. J., & Scott, P. 2009, ARA&A, 47, 481, doi: 10.1146/annurev.astro.46.060407.145222

Beers, T. C. 1987, in Nearly Normal Galaxies. From the Planck Time to the Present, ed. S. M. Faber, 41

Beers, T. C., & Christlieb, N. 2005, ARA&A, 43, 531, doi: 10.1146/annurev.astro.42.053102.134057

Beers, T. C., Preston, G. W., & Shectman, S. A. 1985, AJ, 90, 2089, doi: 10.1086/113917

Beers, T. C., Carollo, D., Ivezić, Ž., et al. 2012, ApJ, 746, 34, doi: 10.1088/0004-637X/746/1/34

Belokurov, V., Sanders, J. L., Fattahi, A., et al. 2020, MNRAS, 494, 3880, doi: 10.1093/mnras/staa876

Bessell, M., Bloxham, G., Schmidt, B., et al. 2011, PASP, 123, 789, doi: 10.1086/660849

Bonaca, A., Conroy, C., Wetzel, A., Hopkins, P. F., & Kereš, D. 2017, ApJ, 845, 101, doi: 10.3847/1538-4357/aa7d0c

Bovy, J., Rix, H.-W., Liu, C., et al. 2012, ApJ, 753, 148, doi: 10.1088/0004-637x/753/2/148

Brown, T. M., Tumlinson, J., Geha, M., et al. 2014, ApJ, 796, 91, doi: 10.1088/0004-637X/796/2/91

Caimmi, R. 2008, New Astronomy, 13, 314–339, doi: 10.1016/j.newast.2007.11.007

Carollo, D., Tissera, P. B., Beers, T. C., et al. 2018, ApJL, 859, L7, doi: 10.3847/2041-8213/aac2dc

Carollo, D., Beers, T. C., Lee, Y. S., et al. 2007, Nature, 450, 1020–1025, doi: 10.1038/nature06460

Carollo, D., Beers, T. C., Chiba, M., et al. 2010, ApJ, 712, 692, doi: 10.1088/0004-637X/712/1/692

Carollo, D., Chiba, M., Ishigaki, M., et al. 2019, ApJ, 887, 22, doi: 10.3847/1538-4357/ab517c

Cenarro, A. J., Moles, M., Cristóbal-Hornillos, D., et al. 2019, A&A, 622, A176, doi: 10.1051/0004-6361/201833036

Chiappini, C., Matteucci, F., & Romano, D. 2001, ApJ, 554, 1044, doi: 10.1086/321427

Chiba, M., & Beers, T. C. 2000, AJ, 119, 2843–2865, doi: 10.1086/301409

Christlieb, N. 2003, Reviews in Modern Astronomy, 16, 191, doi: 10.1002/9783527617647.ch8

Coelho, P. R. T. 2014, MNRAS, 440, 1027, doi: 10.1093/mnras/stu365

Costa-Duarte, M. V., Sampedro, L., Molino, A., et al. 2019, arXiv e-prints, arXiv:1909.08626. https://arxiv.org/abs/1909.08626

Cristobal-Hornillos, et al. 2009, ApJ, 696, 1554, doi: 10.1088/0004-637X/696/2/1554

Cristóbal-Hornillos, D., Varela, J., Ederoclite, A., et al. 2014, in Proc. SPIE, Vol. 9152, Software and Cyberinfrastructure for Astronomy III, 91520O

Da Costa, G. S., Bessell, M. S., Mackey, A. D., et al. 2019, MNRAS, 489, 5900, doi: 10.1093/mnras/stz2550

Dawson, K. S., Schlegel, D. J., Ahn, C. P., et al. 2013, AJ, 145, 10, doi: 10.1088/0004-6256/145/1/10

Demarque, P., Woo, J.-H., Kim, Y.-C., & Yi, S. K. 2004, ApJS, 155, 667, doi: 10.1086/424966

Dietz, S. E., Yoon, J., Beers, T. C., & Placco, V. M. 2020, ApJ, 894, 34, doi: 10.3847/1538-4357/ab7fa4

Eggen, O. J., Lynden-Bell, D., & Sandage, A. R. 1962, ApJ, 136, 748, doi: 10.1086/147433

Eisenstein, D. J., Liebert, J., Harris, H. C., et al. 2006, ApJS, 167, 40, doi: 10.1086/507110

Fenner, Y., & Gibson, B. K. 2003, PASA, 20, 189–195, doi: 10.1071/as02047

Fernández-Alvar, E., Tissera, P. B., Carigi, L., et al. 2019, MNRAS, 485, 1745, doi: 10.1093/mnras/stz443

Foreman-Mackey, D., Hogg, D. W., Lang, D., & Goodman, J. 2013, PASP, 125, 306, doi: 10.1086/670067

Frebel, A., Kirby, E. N., & Simon, J. D. 2010, Nature, 464, 72, doi: 10.1038/nature08772

Gaia Collaboration, Brown, A. G. A., Vallenari, A., et al. 2016, A&A, 595, A2, doi: 10.1051/0004-6361/201629512

Gaia Collaboration, Brown, A. G. A., Vallenari, A., et al. 2018a, A&A, 616, A1, doi: 10.1051/0004-6361/201833051

Gaia Collaboration, Babusiaux, C., van Leeuwen, F., et al. 2018b, A&A, 616, A10, doi: 10.1051/0004-6361/201832843

Gallart, C., Bernard, E. J., Brook, C. B., et al. 2019, Nature Astronomy, 3, 932, doi: 10.1038/s41550-019-0829-5

García Pérez, A. E., Allende Prieto, C., Holtzman, J. A., et al. 2016, AJ, 151, 144, doi: 10.3847/0004-6256/151/6/144

Gattano, C., Andrei, A. H., Coelho, B., et al. 2018, A&A, 614, A140, doi: 10.1051/0004-6361/201732176

Goodman, J., & Weare, J. 2010, Communications in Applied Mathematics and Computational Science, 5, 65, doi: 10.2140/camcos.2010.5.65

Green, G. M., Schlafly, E., Zucker, C., Speagle, J. S., & Finkbeiner, D. 2019, ApJ, 887, 93, doi: 10.3847/1538-4357/ab5362

Hansen, T. T., Andersen, J., Nordström, B., et al. 2016, A&A, 588, A3, doi: 10.1051/0004-6361/201527409

Haywood, M., Di Matteo, P., Lehnert, M. D., et al. 2018, ApJ, 863, 113, doi: 10.3847/1538-4357/aad235

Helmi, A., Babusiaux, C., Koppelman, H. H., et al. 2018, Nature, 563, 85, doi: 10.1038/s41586-018-0625-x

Helmi, A., Irwin, M. J., Tolstoy, E., et al. 2006, ApJL, 651, L121, doi: 10.1086/509784

Ibata, R. A., McConnachie, A., Cuillandre, J.-C., et al. 2017, ApJ, 848, 128, doi: 10.3847/1538-4357/aa855c

Ivezić, Ž., Smith, J. A., Miknaitis, G., et al. 2007, AJ, 134, 973, doi: 10.1086/519976

Jiang, L., Fan, X., Bian, F., et al. 2014, ApJS, 213, 12, doi: 10.1088/0067-0049/213/1/12

Jordi, K., Grebel, E. K., & Ammon, K. 2006, Appl. Phys., 460, 339–347, doi: 10.1051/0004-6361:20066082

Kamada, T., & Kawai, S. 1989, Information Processing Letters, 31, 7 , doi: https://doi.org/10.1016/0020-0190(89)90102-6

Kass, R. E., & Raftery, A. E. 1995, Journal of the American Statistical Association, 90, 773, doi: 10.1080/01621459.1995.10476572

Keller, S., Bessell, M., Schmidt, B., & Francis, P. 2007, Astronomical Society of the Pacific Conference Series, Vol. 364, The SkyMapper Southern Sky Survey, 177

Kim, Y. K., Lee, Y. S., & Beers, T. C. 2019, ApJ, 882, 176, doi: 10.3847/1538-4357/ab3660

Kingma, D. P., & Ba, J. 2014, Adam: A Method for Stochastic Optimization. https://arxiv.org/abs/1412.6980

Kirby, E. N., Simon, J. D., Geha, M., Guhathakurta, P., & Frebel, A. 2008, ApJL, 685, L43, doi: 10.1086/592432

Kotoneva, E., Flynn, C., Chiappini, C., & Matteucci, F. 2002, MNRAS, 336, 879, doi: 10.1046/j.1365-8711.2002.05825.x

Lee, Y. S., Beers, T. C., & Kim, Y. K. 2019, ApJ, 885, 102, doi: 10.3847/1538-4357/ab4791

Lee, Y. S., Beers, T. C., Kim, Y. K., et al. 2017, ApJ, 836, 91, doi: 10.3847/1538-4357/836/1/91

Lee, Y. S., Beers, T. C., Sivarani, T., et al. 2008a, AJ, 136, 2022, doi: 10.1088/0004-6256/136/5/2022

—. 2008b, AJ, 136, 2050, doi: 10.1088/0004-6256/136/5/2050

Lee, Y. S., Beers, T. C., Masseron, T., et al. 2013, AJ, 146, 132, doi: 10.1088/0004-6256/146/5/132

Li, H. N., Christlieb, N., Schörck, T., et al. 2010, A&A, 521, A10, doi: 10.1051/0004-6361/201014797

López-Sanjuan, C., Varela, J., Cristóbal-Hornillos, D., et al. 2019, arXiv e-prints, arXiv:1907.12939. https://arxiv.org/abs/1907.12939

Majewski, S. R., Schiavon, R. P., Frinchaboy, P. M., et al. 2017, AJ, 154, 94, doi: 10.3847/1538-3881/aa784d

Marín-Franch, A., Chueca, S., Moles, M., et al. 2012, in Proc. SPIE, Vol. 8450, Modern Technologies in Space- and Ground-based Telescopes and Instrumentation II, 84503S

Marrese, P. M., Marinoni, S., Fabrizio, M., & Altavilla, G. 2019, A&A, 621, A144, doi: 10.1051/0004-6361/201834142

Mendes de Oliveira, C., Ribeiro, T., Schoenell, W., et al. 2019, MNRAS, 489, 241, doi: 10.1093/mnras/stz1985

Mészáros, S., Holtzman, J., García Pérez, A. E., et al. 2013, AJ, 146, 133, doi: 10.1088/0004-6256/146/5/133

Mints, A., & Hekker, S. 2019, A&A, 621, A17, doi: 10.1051/0004-6361/201834256

Molino, A., Benítez, N., Moles, M., et al. 2014, MNRAS, 441, 2891, doi: 10.1093/mnras/stu387

Placco, V. M., Frebel, A., Beers, T. C., & Stancliffe, R. J. 2014, ApJ, 797, 21, doi: 10.1088/0004-637X/797/1/21

Placco, V. M., Beers, T. C., Santucci, R. M., et al. 2018, AJ, 155, 256, doi: 10.3847/1538-3881/aac20c

Prantzos, N. 2007, in EAS Publications Series, Vol. 24, EAS Publications Series, ed. E. Emsellem, H. Wozniak, G. Massacrier, J. F. Gonzalez, J. Devriendt, & N. Champavert, 3–14

Rockosi, C., Beers, T. C., Majewski, S., Schiavon, R., & Eisenstein, D. 2009, in astro2010: The Astronomy and Astrophysics Decadal Survey, Vol. 2010, 14

Ryan, S. G., & Norris, J. E. 1991, AJ, 101, 1865, doi: 10.1086/115812

Sahlholdt, C. L., Casagrande, L., & Feltzing, S. 2019, ApJL, 881, L10, doi: 10.3847/2041-8213/ab321e

Salvadori, S., Ferrara, A., & Schneider, R. 2008, MNRAS,
    386, 348, doi: 10.1111/j.1365-2966.2008.13035.x

Scannapieco, C., Tissera, P. B., White, S. D. M., &
    Springel, V. 2005, MNRAS, 364, 552,
    doi: 10.1111/j.1365-2966.2005.09574.x

Scannapieco, C., White, S. D. M., Springel, V., & Tissera,
    P. B. 2009, MNRAS, 396, 696,
    doi: 10.1111/j.1365-2966.2009.14764.x

Scannapieco, E., Kawata, D., Brook, C. B., et al. 2006,
    ApJ, 653, 285, doi: 10.1086/508487

Schlafly, E. F., & Finkbeiner, D. P. 2011, ApJ, 737, 103,
    doi: 10.1088/0004-637X/737/2/103

Schlegel, D. J., Finkbeiner, D. P., & Davis, M. 1998, ApJ,
    500, 525, doi: 10.1086/305772

Schörck, Christlieb, N., Cohen, J. G., et al. 2009, A&A,
    507, 817, doi: 10.1051/0004-6361/200810925

Searle, L., & Zinn, R. 1978, ApJ, 225, 357,
    doi: 10.1086/156499

Simon, J. D. 2019, ARA&A, 57, 375,
    doi: 10.1146/annurev-astro-091918-104453

Springel, V., Wang, J., Vogelsberger, M., et al. 2008,
    MNRAS, 391, 1685,
    doi: 10.1111/j.1365-2966.2008.14066.x

Starkenburg, E., Martin, N., Youakim, K., et al. 2017,
    MNRAS, 471, 2587, doi: 10.1093/mnras/stx1068

Suda, T., Katsuta, Y., Yamada, S., et al. 2008, PASJ, 60,
    1159, doi: 10.1093/pasj/60.5.1159

Thomas, G. F., Annau, N., McConnachie, A., et al. 2019,
    ApJ, 886, 10, doi: 10.3847/1538-4357/ab4a77

Tissera, P. B., Beers, T. C., Carollo, D., & Scannapieco, C.
    2014, MNRAS, 439, 3128, doi: 10.1093/mnras/stu181

Tissera, P. B., Machado, R. E. G., Carollo, D., et al. 2018,
    MNRAS, 473, 1656, doi: 10.1093/mnras/stx2431

Tissera, P. B., Scannapieco, C., Beers, T. C., & Carollo, D.
    2013, MNRAS, 432, 3391, doi: 10.1093/mnras/stt691

Tissera, P. B., White, S. D. M., & Scannapieco, C. 2012,
    MNRAS, 420, 255, doi: 10.1111/j.1365-2966.2011.20028.x

Tolstoy, E., Hill, V., & Tosi, M. 2009, ARA&A, 47, 371,
    doi: 10.1146/annurev-astro-082708-101650

Whitten, D. D., Placco, V. M., Beers, T. C., et al. 2019a,
    A&A, 622, A182, doi: 10.1051/0004-6361/201833368

Whitten, D. D., Beers, T. C., Placco, V. M., et al. 2019b,
    ApJ, 884, 67, doi: 10.3847/1538-4357/ab4269

Whitten, D. D., Placco, V. M., Beers, T. C., et al. 2019c,
    A&A, 622, A182, doi: 10.1051/0004-6361/201833368

Wilson, E. B. 1927, Journal of the American Statistical
    Association, 22, 209,
    doi: 10.1080/01621459.1927.10502953

Wolf, C., Onken, C. A., Luvaul, L. C., et al. 2018, PASA,
    35, e010, doi: 10.1017/pasa.2018.5

Yanny, B., Rockosi, C., Newberg, H. J., et al. 2009, AJ,
    137, 4377, doi: 10.1088/0004-6256/137/5/4377

Yoon, J., Whitten, D. D., Beers, T. C., et al. 2020, APJj,
    894, 7, doi: 10.3847/1538-4357/ab7daf

Yoon, J., Beers, T. C., Placco, V. M., et al. 2016, ApJ, 833,
    20, doi: 10.3847/0004-637X/833/1/20

Yoon, J., Beers, T. C., Dietz, S., et al. 2018, ApJ, 861, 146,
    doi: 10.3847/1538-4357/aaccea

York, D. G., Adelman, J., Anderson, John E., J., et al.
    2000, AJ, 120, 1579, doi: 10.1086/301513

Youakim, K., Starkenburg, E., Martin, N. F., et al. 2020,
    MNRAS, 492, 4986, doi: 10.1093/mnras/stz3619

7. APPENDIX

In this section, we provide figures relevant to the calibrations for SPHINX. In Figure 14, the residuals for effective temperature, metallicity, and absolute carbon abundance are shown, determined with an independent validation set during the training procedures for SPHINX, as described in the text.
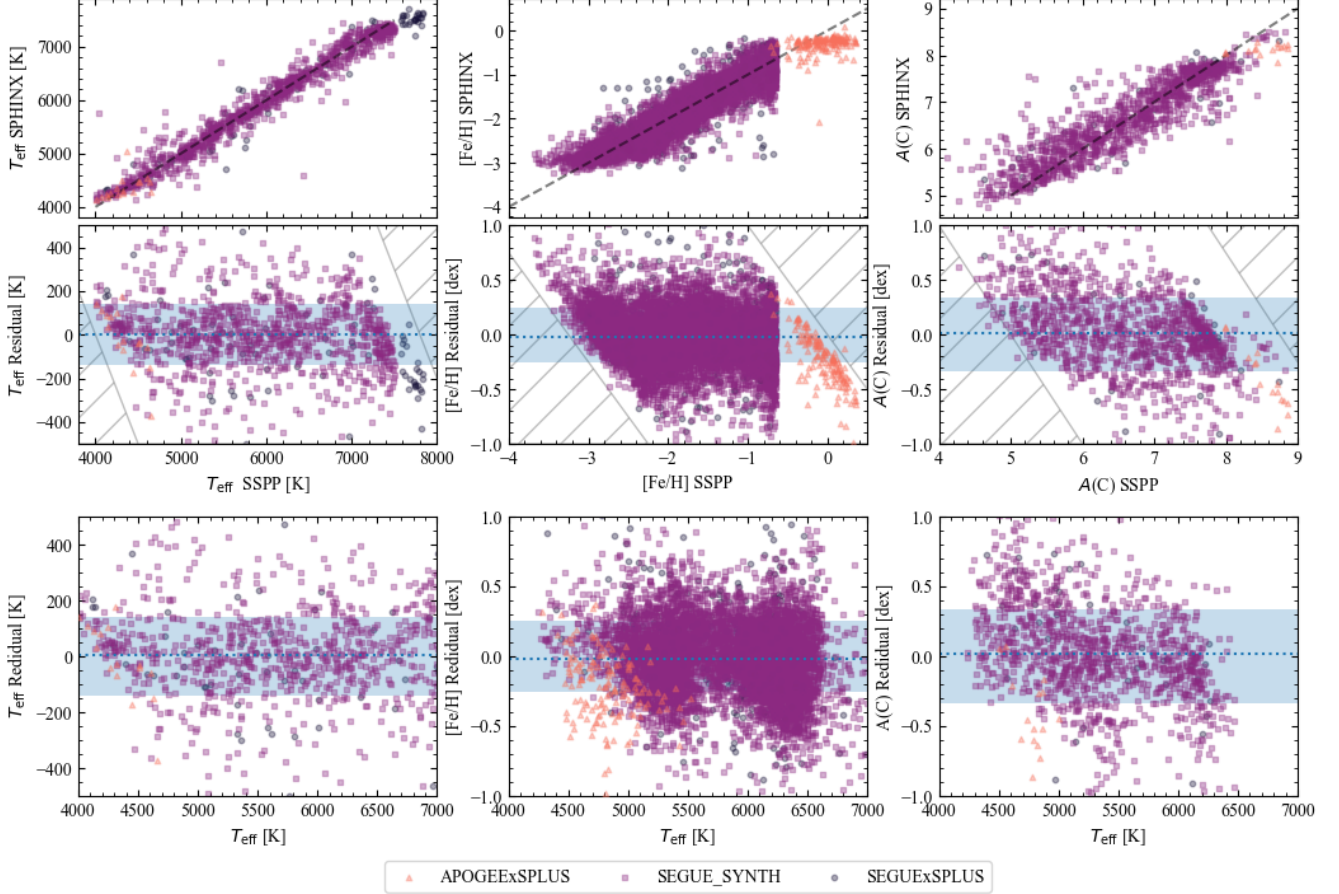

Figure 14. Photometric estimates of effective temperature are shown in the left panels, with metallcity and absolute carbon abundance in the center and right panels, respectively. All results are produced by SPHINX using S-PLUS photometry. In the bottom panels, residuals are shown of effective temperature, metallicity, and absolute carbon abundance, as a function of the spectroscopic effective temperature estimate from the n-SSPP estimates of SEGUE and APOGEE stars.